nature plants

Article

https://doi.org/10.1038/s41477-025-02137-z

RNA m^{6}A regulates the transcription and heterochromatin state of retrotransposons in *Arabidopsis*

Received: 19 July 2024

Accepted: 21 September 2025

Published online: 24 October 2025

Check for updates

Peizhe Song[1,4], Zhihe Cai[1,4], Subiding Tayier[1,4], Enlin Tian[1], Zixin Chen[1], Kemiao Yu[2], Lixiang Liu[1] & Guifang Jia[1,2,3]

Chromatin and transcription states are crucial for establishing and maintaining gene regulation and genome integrity, governed by a complex network of epigenetic modifications. Despite significant advancements, the interplay between epitranscriptomic and epigenetic modifications in transcriptional regulation and chromatin state remains elusive in plants. Here we profile a comprehensive spectrum of N^6-methyladenosine (m^{6}A) on chromatin-associated RNAs, especially retrotransposon transcripts, in *Arabidopsis*. We show that m^{6}A writer subunits FIP37 and VIR mediate the methylation of retrotransposon RNAs, which are recognized by the nuclear m^{6}A reader proteins CPSF30-L and ECT12, leading to a closed heterochromatin state and transcription suppression of m^{6}A retrotransposon RNAs. Through monitoring nuclear RNA stability and transcription rate upon the depletion of either writer or reader, we provide evidence consistent with a model in which CPSF30-L associates with SUVH4/5/6 and ATXR5/6 and contributes to histone H3 K9 dimethylation and H3 K27 monomethylation at m^{6}A-marked retrotransposons. Our findings elucidate a regulatory mechanism involving RNA m^{6}A formation and recognition, coupled with histone modifications, thereby highlighting the intricate epitranscriptomic and epigenetic interplay in plant physiological and biological processes.

Over 170 types of RNA modifications have been identified across all kingdoms of life. N^6-methyladenosine (m^{6}A) is the most widespread and highly conserved modification in mRNAs and noncoding RNAs (ncRNAs)[1]. In *Arabidopsis*, m^{6}A is co-transcriptionally incorporated into RNA transcripts by the MTA–MTB complex and several accessory subunits[2–4], erased by demethylases ALKBH9B/10B[5,6] and recognized by readers such as YTH-domain-containing proteins[7–13]. The m^{6}A modification regulates many critical post-transcriptional processes in the cytoplasm and nucleus in both plants and mammals, such as mRNA stability, RNA–protein granule formation, alternative polyadenylation and the resolution of R-loops[8–11,13,14]. Additionally, chromatin states and transcription can be modulated by m^{6}A methylation in critical nuclear RNAs, especially chromatin-associated regulatory RNAs, in mammalian cells[15–19]. These studies suggest that m^{6}A modification in different RNA types plays distinctive roles in the epitranscriptomic regulation of gene expression.

Transposons are DNA molecules capable of moving from one location to another and are widespread in most eukaryotic genomes[20].

[1]Synthetic and Functional Biomolecules Center, Beijing National Laboratory for Molecular Sciences, Key Laboratory of Bioorganic Chemistry and Molecular Engineering of Ministry of Education, College of Chemistry and Molecular Engineering, Peking University, Beijing, China. [2]Peking-Tsinghua Center for Life Sciences, Peking University, Beijing, China. [3]Beijing Advanced Center of RNA Biology (BEACON), Peking University, Beijing, China. [4]These authors contributed equally: Peizhe Song, Zhihe Cai, Subiding Tayier. e-mail: guifangjia@pku.edu.cn

Retrotransposons, classified as class I transposons, proliferate through reverse transcription of RNA intermediates and comprise over 40% and 70% of the human and maize genomes, respectively[21–23]. Due to their potentially adverse effects on host genomes, most transposons are extensively repressed by epigenetic marks, including DNA methylation and histone modifications. Plants and mammals exhibit striking divergence in heterochromatin-associated histone modifications: histone H3 K9 dimethylation and H3 K27 monomethylation serve as heterochromatin marks in plants, whereas mammals primarily use H3 K9 trimethylation for heterochromatin assembly, with H3 K9 dimethylation predominantly marking euchromatic regions[24,25]. Recent independent studies have revealed that METTL3-mediated m^{6}A methylation on retrotransposons orchestrates with H3 K9 trimethylation to maintain heterochromatin formation, thereby regulating retrotransposon repression and preserving embryonic stem cell identity[18,26]. FTO-mediated m^{6}A demethylation on LINE1 RNA regulates its abundance and the local chromatin state during mouse oocyte and embryonic development[16]. Moreover, the expression of human FTO in rice demethylates m^{6}A and promotes chromatin accessibility and transcriptional activation[27], suggesting that plant endogenous m^{6}A modification might play a role in regulating chromatin state and transcription. However, it remains unknown whether and how m^{6}A regulates chromatin state and transcription in plants.

Here we optimized m^{6}A antibody immunoprecipitation sequencing (m^{6}A-Seq) for plant chromatin-associated RNA (caRNA) and profiled the methylome landscape of retrotransposons in *Arabidopsis*. m^{6}A methylation on retrotransposon RNAs, deposited by m^{6}A writers, is recognized by the nuclear m^{6}A reader protein CPSF30-L. CPSF30-L physically interacts with histone methylation writers SUVH4/5/6 and ATXR5/6 to increase the repressive histone marks H3 K9 dimethylation and H3 K27 monomethylation in the local heterochromatin region, leading to closed chromatin accessibility and transcription suppression. Moreover, ECT12 is characterized as another nuclear m^{6}A reader protein, which interacts with CPSF30-L and redundantly regulates retrotransposon RNA transcription and the local heterochromatic histone levels. Our results uncover a layer of epigenetic regulation in which RNA methylation couples with histone modifications to ensure silenced transcription and heterochromatin integrity in plants.

Results

Landscape of m^{6}A retrotransposon RNAs revealed via caRNA m^{6}A-Seq in *Arabidopsis*

To unveil the transcriptional spectrum of m^{6}A-methylated RNA molecules, we optimized m^{6}A-Seq suitable for plant caRNA, referred to as caRNA m^{6}A-Seq (Fig. 1a). This method was developed on the basis of the efficient isolation of non-DNA-contaminated and non-ribosomal caRNAs followed by m^{6}A immunoprecipitation (m^{6}A-IP) (Fig. 1b and Supplementary Fig. 1a,b). We also incorporated m^{6}A spike-in and External RNA Controls Consortium (ERCC) spike-ins to calibrate the efficiency of m^{6}A-IP and the variability of expression levels, respectively.

To compare the m^{6}A profiles of transcriptional transcriptomes and steady-state transcriptomes, we conducted parallel extractions of caRNAs and processed mRNAs (poly(A)$^+$ RNAs) from two biological replicates of six-day-old wild-type (WT) seedlings and performed caRNA m^{6}A-Seq and canonical m^{6}A-Seq. Correlation analysis of paired input and m^{6}A-IP sets between caRNAs and poly(A)$^+$ RNAs was conducted independently for each set (Supplementary Fig. 1c). Considering that newly transcribed transcripts contain processing intermediates, we classified the reads into exonic, intronic, exon/intron junction and intergenic categories. Notably, caRNA sequencing (caRNA-Seq) revealed a more than fivefold higher occupancy of reads in intronic, exon/intron junction and intergenic regions compared with poly(A)$^+$ RNA (Fig. 1c and Supplementary Fig. 1d), suggesting that caRNA m^{6}A-Seq can specifically capture nascent transcripts. On the basis of the analysis criteria (false discovery rate < 0.05), 11,466 and 11,227 m^{6}A peaks were exclusively detected in caRNAs and poly(A)$^+$ RNAs, respectively (Supplementary Fig. 1e and Supplementary Tables 1 and 2).

Comparing identified m^{6}A sites between caRNAs and poly(A)$^+$ RNAs, we observed an increased number of m^{6}A peaks in exonic regions in caRNA m^{6}A-Seq (Fig. 1d). This difference may be attributed to variations in transcript composition, particularly the enrichment of nascent RNAs in which RNA Polymerase II (Pol II) has not yet completed transcription of the full 3′ untranslated region (UTR), as well as insufficient m^{6}A demethylation during transcription. Moreover, we observed that a high number of m^{6}A peaks were enriched in transposon RNAs and other noncoding RNA regions (Fig. 1d and Supplementary Fig. 1f). We computationally interrogated the m^{6}A levels of these three caRNA types with spike-ins for calibration. Intriguingly, the m^{6}A levels of transposon RNAs are higher than those of pre-mRNAs and ncRNAs (Fig. 1e).

Retrotransposons and DNA transposons are the two primary classes of transposable elements. Through caRNA m^{6}A-Seq analysis, we identified 242 m^{6}A peaks on retrotransposon RNAs and 67 on DNA transposon RNAs (Supplementary Fig. 1g). We also observed that retrotransposons are transcribed more actively (Supplementary Fig. 1h), underscoring the preferential involvement of m^{6}A in retrotransposon RNA regulation. Interrogating a comprehensive methylome profiling of m^{6}A in poly(A)$^+$ RNAs and caRNAs, we identified a total of 139 annotated m^{6}A-modified retrotransposon RNAs (referred to as m^{6}A retrotransposon RNAs) due to the low expression of retrotransposon RNAs (Supplementary Table 3). These m^{6}A retrotransposon RNAs are predominantly localized at pericentromeric heterochromatin regions (Supplementary Fig. 1i). Unlike the typical accumulation of m^{6}A in the 3′ UTR of mRNA, m^{6}A was distributed across the entire transcripts, with particularly high enrichment at the 5′ and 3′ ends of retrotransposon transcripts (Fig. 1f and Supplementary Fig. 1j,k). Motif analysis clustering all m^{6}A peaks in retrotransposon RNA identified the WAC (W indicates A or U) motif, consistent with the canonical RAC (R indicates A or G) motif found in mRNAs (Supplementary Fig. 1l). Additionally, m^{6}A retrotransposon RNAs exhibited GAG or SAU (S indicates G or C) motifs (Supplementary Fig. 1l), resembling the GAAGG and GGAUU non-canonical motifs found in mammalian retrotransposon RNAs[26].

Retrotransposons include long-terminal-repeat (for example, *COPIA* and *GYPSY*) and non-long-terminal-repeat retrotransposons (for example, *LINE* and *SINE*)[28]. We observed that *COPIA*, *GYPSY* and *LINE* retrotransposons harbour 108, 88 and 43 m^{6}A peaks, corresponding to 48, 61 and 24 transcripts, respectively, whereas *SINE* displays fewer m^{6}A peaks (Fig. 1g, Supplementary Fig. 1m,n and Supplementary Table 3). m^{6}A-IP followed by quantitative PCR (m^{6}A-IP–qPCR) using *COPIA62* and *COPIA66* as representative examples confirmed authentic m^{6}A enrichment in these identified peak regions but not elsewhere (Fig. 1h,i). The high detectability of methylation on nascent retrotransposon RNAs enables us to explore the role and mechanism of m^{6}A in transcriptional regulation.

m^{6}A is deposited on retrotransposon RNA transcribed by Pol II and Pol V

Since m^{6}A is deposited co-transcriptionally during RNA polymerase transcription, we first investigated which polymerase is responsible for retrotransposon transcription. Unlike mammals, which possess only Pol I, Pol II and Pol III, plants have uniquely evolved two additional RNA polymerases, Pol IV and Pol V[29]. Pol I is involved in rRNA transcription; Pol II transcribes mRNAs and certain ncRNAs; Pol III synthesizes 5S rRNA, tRNA and other small RNAs; Pol IV produces ~30–40-nucleotide transcripts, primarily from repetitive regions; and Pol V generates noncoding transcripts, mainly from heterochromatic regions[30–32]. We performed caRNA-Seq using six-day-old seedlings of the WT line,

https://doi.org/10.1038/s41477-025-02137-z

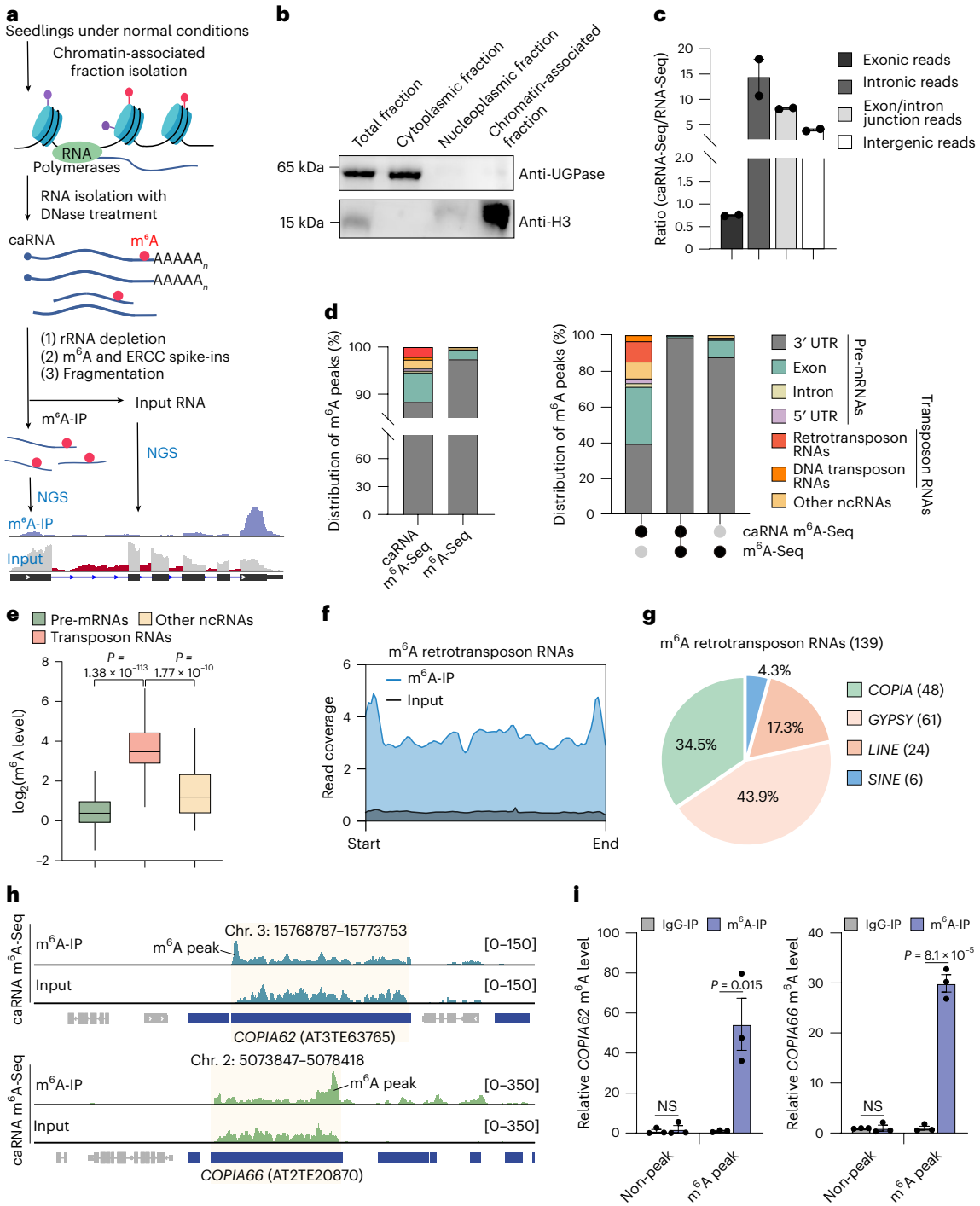

Fig. 1 | m^{6}A methylome profiling on retrotransposon RNAs in *Arabidopsis*. **a**, The caRNA m^{6}A-Seq method suitable for plant research. NGS, next-generation sequencing. **b**, Cell fractionation validation shown via immunoblot analysis. UDP-glucose pyrophosphorylase (UGPase) and H3 were used as cytoplasmic and nuclear protein markers, respectively. **c**, Ratio of reads in caRNA-Seq versus RNA-Seq libraries mapped to exons, introns, exon/intron junctions or intergenic regions. The data are presented as mean ± s.e.m. ($n = 2$ independent experiments). **d**, Distribution of m^{6}A peaks at distinct genomic regions including 3′ UTRs, exons, introns, 5′ UTRs, retrotransposon RNAs, DNA transposon RNAs and other ncRNAs annotated from TAIR (https://www.arabidopsis.org/) in caRNA m^{6}A-Seq and poly(A)$^+$ m^{6}A-Seq (m^{6}A-Seq). m^{6}A peaks were categorized into three groups: m^{6}A peaks detected only in caRNA m^{6}A-Seq, m^{6}A peaks detected in both caRNA and m^{6}A-Seq, and m^{6}A peaks detected only in m^{6}A-Seq. **e**, Box plot showing m^{6}A levels of m^{6}A-marked pre-mRNAs, transposon RNAs and other ncRNAs. The medians (horizontal lines), interquartile ranges (boxes), and ±1.5× the interquartile range (whiskers) of the data are shown ($n = 10{,}438$, 201 and 38 annotated pre-mRNAs, transposon RNAs and ncRNAs, respectively). *P* values were determined using paired two-sided Wilcoxon tests. **f**, Metagene plot of caRNA m^{6}A-Seq read density over m^{6}A retrotransposon RNAs. **g**, Pie chart depicting the types of m^{6}A retrotransposon RNAs. **h**, Genomic visualization showing the normalized read densities of m^{6}A methylation and input from caRNA m^{6}A-Seq on the representative loci *COPIA62* and *COPIA66*. Blue and grey transcripts indicate transposon and protein-coding RNAs, respectively. **i**, m^{6}A-IP–qPCR validation of the m^{6}A peaks in *COPIA62* and *COPIA66*. The data are presented as mean ± s.e.m. ($n = 3$ independent experiments). The *P* values are from two-tailed Student's *t*-tests. NS, not significant.

a line carrying the weak Pol II mutant allele *nrpb2-3* (ref. 33) and the Pol V mutant *nrpe1-11* (ref. 34) to examine whether the expression levels of retrotransposon RNAs are controlled by Pol II and Pol V. We found that the expression levels of certain retrotransposon RNAs, regardless of m^{6}A modification, were decreased in both *nrpb2-3* and *nrpe1-11* mutants, while some expression levels were specifically reduced in *nrpb2-3* or *nrpe1-11* (Supplementary Fig. 2a–d and Supplementary Table 4). Our results revealed that retrotransposon transcription is finely regulated by Pol II and Pol V occupancy, with both polymerases coordinately and specifically modulating the transcription of these RNAs.

Considering the distinct RNA products transcribed by each polymerase, we analysed Pol II and Pol V occupancy levels across m^{6}A and non-m^{6}A retrotransposon RNAs using published data from chromatin immunoprecipitation followed by sequencing (ChIP–Seq)[35,36]. We observed that both Pol II and Pol V exhibit higher binding abundance on m^{6}A retrotransposons than on non-m^{6}A retrotransposons, which aligns with the higher expression levels of m^{6}A retrotransposon RNAs than those of non-m^{6}A retrotransposons (Supplementary Fig. 2e,f), indicating that m^{6}A is deposited on highly expressed transcripts. Furthermore, to examine whether m^{6}A is deposited on transcripts transcribed by Pol II and Pol V, we performed formaldehyde-crosslinking-assisted RNA immunoprecipitation (FA-RIP) and quantified m^{6}A levels on Pol-II- and Pol-V-bound transcripts using Pol II antibody in six-day-old WT seedlings and for Pol V using anti-GFP beads in six-day-old *NRPE1*::*NRPE1-GFP nrpe1-11* seedlings. The results showed that m^{6}A was significantly enriched in Pol II- and Pol V-bound transcripts compared with the input and immunoglobulin G (IgG) control portions, providing direct evidence that m^{6}A is deposited on both Pol-II and Pol-V-transcribed transcripts (Supplementary Fig. 2g).

The m^{6}A modification on retrotransposon RNAs deposited by the MTA–MTB writer complex represses the expression of retrotransposon RNAs

To investigate the m^{6}A-mediated regulatory functions of retrotransposons in *Arabidopsis*, we employed the subunit mutants of the m^{6}A MTA–MTB writer complex: *fip37-4 LEC1*::*FIP37* and *vir*[37], which cause a nearly 90% reduction in m^{6}A levels in poly(A)$^+$ RNA (Supplementary Fig. 3a). We performed caRNA m^{6}A-Seq on six-day-old *fip37-4 LEC1*::*FIP37* and *vir* mutants with two biological replicates, ensuring high replicability between the replicates (Supplementary Fig. 3b and Supplementary Tables 5 and 6). Compared with WT plants, the disruption of m^{6}A writer function in either *fip37-4 LEC1*::*FIP37* or *vir* globally reduced total m^{6}A levels and m^{6}A peaks in pre-mRNAs, retrotransposon RNAs and other ncRNAs (Fig. 2a and Supplementary Fig. 3c–e), suggesting that the MTA–MTB writer complex is responsible for m^{6}A installation on these RNAs. Almost all m^{6}A modifications on retrotransposon RNAs were dramatically decreased in both *fip37-4 LEC1*::*FIP37* and *vir* (Supplementary Fig. 3f). Furthermore, expression level analysis revealed that over 80% of m^{6}A retrotransposon RNAs were upregulated in *fip37-4 LEC1*::*FIP37* and *vir* (Supplementary Fig. 3g). In contrast to the minimal changes in m^{6}A DNA transposon RNA expression, the abundance of m^{6}A-modified retrotransposon RNAs, but not non-m^{6}A ones, was significantly increased upon the depletion of either FIP37 or VIR (Fig. 2b,c, Supplementary Fig. 3h–k and Supplementary Table 7). To confirm the reliability of m^{6}A-writer-mediated regulation of retrotransposon RNAs, we independently conducted caRNA-Seq on six-day-old WT, *fip37-4 LEC1*::*FIP37* and *vir* seedlings with two biological replicates, which showed consistent results (Supplementary Fig. 3l–n).

We further examined the correlation between m^{6}A and expression levels across the classified types of retrotransposon RNAs. Retrotransposon RNAs in the *COPIA*, *GYPSY* and *LINE* families, as well as their transcriptionally active subfamilies, displayed lower m^{6}A methylation levels and higher expression levels in either *fip37-4 LEC1*::*FIP37* or *vir* than in WT plants (Fig. 2d). The elevated expression levels of these retrotransposon RNAs were positively correlated with the decreased m^{6}A methylation level caused by either FIP37 or VIR depletion (Fig. 2e). Moreover, m^{6}A-IP–qPCR and qPCR assays were performed to validate the m^{6}A-mediated negative regulation of *COPIA22* and *ATRE1* transcripts (Fig. 2f–h). Taken together, these results suggest that the MTA–MTB writer complex is required for retrotransposon m^{6}A deposition, and m^{6}A methylation suppresses retrotransposon RNA abundance.

CPSF30-L binds and suppresses the expression of m^{6}A retrotransposon RNAs

The mechanism by which m^{6}A guides and decides RNA fate is determined by its reader proteins[38,39]. In *Arabidopsis*, CPSF30-L has been characterized as the nuclear m^{6}A reader[9,10]. Its co-expression patterns with *FIP37* and *VIR*, along with its nuclear localization, suggest a potential role in binding m^{6}A retrotransposon RNAs (Supplementary Fig. 4a). To determine whether the m^{6}A-binding function of CPSF30-L regulates the expression of these RNAs, we performed two biological replicates of caRNA-Seq using six-day-old seedlings from WT, *cpsf30-l* and two complementation lines respectively expressing WT CPSF30-L (*CPSF30*::*CPSF30-L cpsf30-l*, termed *CPSF30-L*) and the CPSF30-L(W259A/W310A) mutant with disrupted m^{6}A-binding capability (*CPSF30*::*CPSF30-Lm cpsf30-l*, termed *CPSF30-Lm*) in the *cpsf30-l* background[10]. The pairwise correlation between the WT and *CPSF30-L*, as well as between *cpsf30-l* and *CPSF30-Lm*, showed high reproducibility (Supplementary Fig. 4b). In line with the results obtained when depleting m^{6}A methyltransferase subunits (Fig. 2b,c), we observed a substantial increase in the abundance of m^{6}A retrotransposon RNAs and typical retrotransposon subfamilies in the *cpsf30-l* mutant (Fig. 3a–c). Importantly, the alterations observed in *cpsf30-l* were rescued by expressing CPSF30-L but not the m^{6}A-binding-function-abolished CPSF30-Lm (Fig. 3a–c, Supplementary Fig. 4c,d and Supplementary Table 8). We also compared the expression levels of m^{6}A and non-m^{6}A retrotransposon RNAs, revealing that the expression levels of m^{6}A-modified transcripts, but not non-m^{6}A RNAs, were significantly higher in both *cpsf30-l* and *CPSF30-Lm* than in WT and *CPSF30-L* plants (Supplementary Fig. 4e). Furthermore, the increased expression levels of m^{6}A retrotransposon RNAs in *cpsf30-l* and *CPSF30-Lm* plants exhibited a positive correlation with their m^{6}A methylation levels (Fig. 3d). These results suggest that the m^{6}A-binding function of CPSF30-L suppresses the expression levels of m^{6}A retrotransposon RNAs.

Given the nuclear subcellular localization of CPSF30-L, we exploited nuclear enrichment in combination with formaldehyde cross-linking and immunoprecipitation (nuclear FA-CLIP) in six-day-old *CPSF30-L* and *CPSF30-Lm* seedlings (Supplementary Fig. 4f). Compared with standard FA-CLIP, nuclear FA-CLIP demonstrated more effective enrichment of m^{6}A-modified RNA in the CPSF30-L-IP fraction (Supplementary Fig. 4g). Clustering analysis of two biological replicates confirmed the reproducibility of our nuclear FA-CLIP sequencing data (Supplementary Fig. 4h). CPSF30-L displayed significantly higher binding intensity to m^{6}A-modified retrotransposon RNAs than to non-m^{6}A RNAs (Fig. 3e). As illustrated in nuclear FA-CLIP and caRNA-Seq, CPSF30-L specifically bound to the m^{6}A modification on *COPIA22* and *ATRE1* and mediated their expression (Fig. 3f). FA-RIP-qPCR and qPCR assays further confirmed that CPSF30-L directly binds to retrotransposon RNAs and suppresses their abundance in an m^{6}A-dependent manner (Fig. 3g,h).

We also overlapped the upregulated m^{6}A retrotransposon RNAs in m^{6}A writer mutants (*fip37-4 LEC1*::*FIP37* and *vir*) with those in m^{6}A reader mutants (*cpsf30-l* and *CPSF30-Lm*). The results showed that the depletion of m^{6}A writer subunits FIP37 and VIR, and m^{6}A reader CPSF30-L, increases the expression of the majority of m^{6}A retrotransposon RNAs (Fig. 3i). This further supports the notion that m^{6}A methylation on retrotransposon RNAs, recognized by CPSF30-L, contributes to suppressing the expression of these RNAs.

https://doi.org/10.1038/s41477-025-02137-z

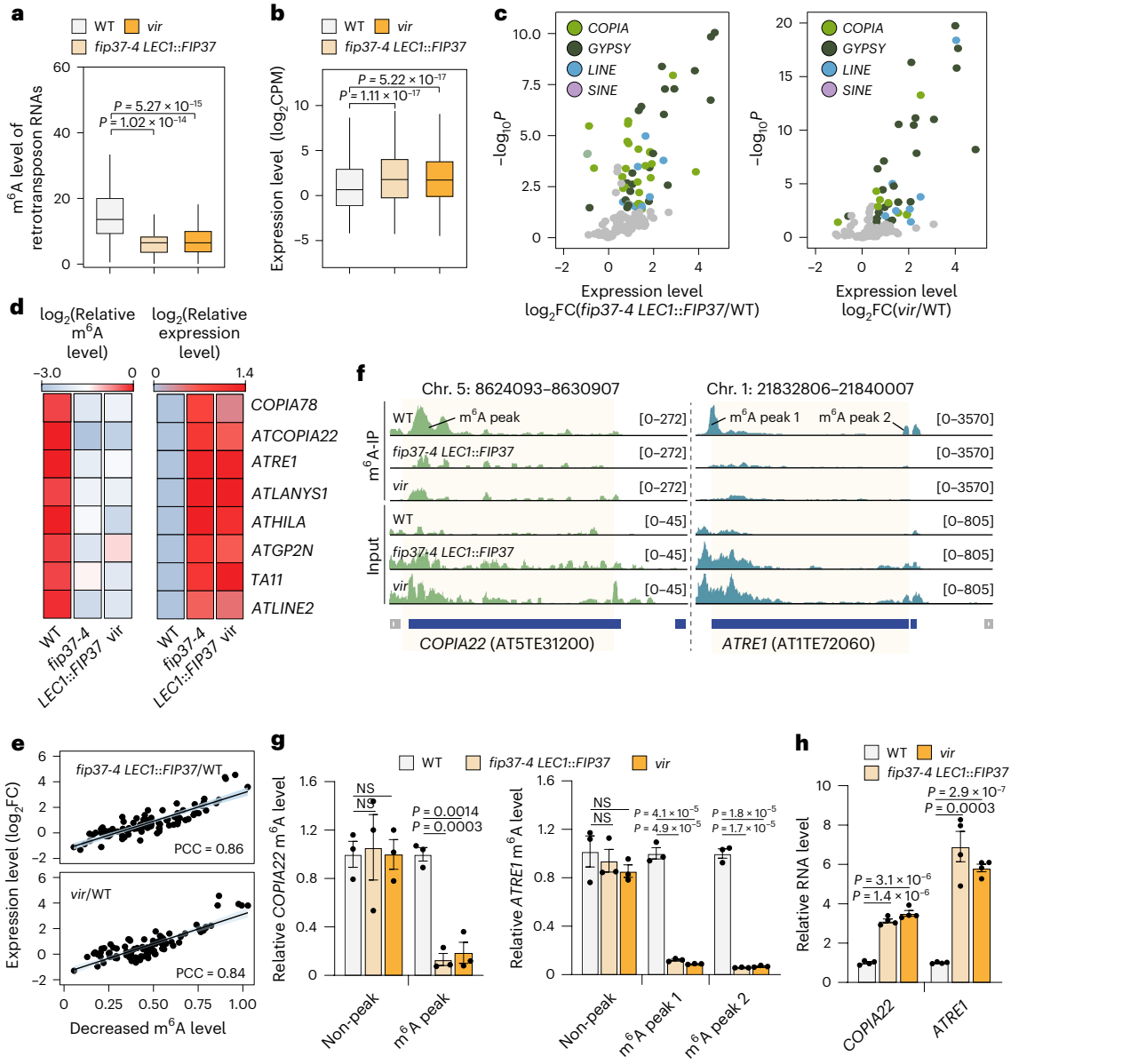

Fig. 2 | m^{6}A writers regulate retrotransposon m^{6}A methylation and retrotransposon repression. a, Box plot showing the m^{6}A levels of retrotransposon RNAs in WT, *fip37-4 LEC1*::*FIP37* and *vir* seedlings. The medians (horizontal lines), interquartile ranges (boxes), and ±1.5× the interquartile range (whiskers) of the data are shown (n = 139 m^{6}A retrotransposon RNAs). P values were determined using paired two-sided Wilcoxon tests. **b**, Box plot showing the expression levels of m^{6}A retrotransposon RNAs in WT, *fip37-4 LEC1*::*FIP37* and *vir* seedlings. The medians (horizontal lines), interquartile ranges (boxes), and ±1.5× the interquartile range (whiskers) of the data are shown (n = 139 m^{6}A retrotransposon RNAs). P values were determined using paired two-sided Wilcoxon tests. **c**, Volcano plots showing expression level changes of m^{6}A retrotransposon RNAs upon either *FIP37* (left) or *VIR* (right) depletion. Light green, dark green, blue and purple denote significantly dysregulated m^{6}A retrotransposon RNAs belonging to *COPIA*, *GYPSY*, *LINE* and *SINE*, respectively. Grey denotes non-differentially expressed m^{6}A retrotransposon RNAs. FC, fold change. P values were calculated via a two-sided negative binomial generalized linear model from the count data. The threshold is $\log_2$FC > 0.58 with P < 0.05. **d**, Heat map showing changes in relative m^{6}A and expression levels of the indicated m^{6}A retrotransposon subfamilies in WT, *fip37-4 LEC1*::*FIP37* and *vir* seedlings. **e**, Scatter plots showing the positive correlation between decreased m^{6}A levels and expression change of m^{6}A retrotransposon RNAs upon either *FIP37* (top) or *VIR* (bottom) depletion. The light-blue region indicates the 95% confidence interval. PCC, Pearson's correlation coefficient. **f**, Genomic visualization showing the normalized read densities of m^{6}A methylation and input from the WT, *fip37-4 LEC1*::*FIP37* and *vir* on the representative loci *COPIA22* and *ATRE1*. Blue and grey transcripts indicate transposon and protein-coding RNAs, respectively. **g**, m^{6}A-IP–qPCR analysis of m^{6}A levels on the *COPIA22* and *ATRE1* loci in the indicated 6-day-old seedlings. m^{6}A levels are shown relative to those in the WT. The data are presented as mean ± s.e.m. (n = 3 independent experiments). The P values are from two-tailed Student's t-tests. **h**, Relative expression levels of *COPIA22* and *ATRE1* in the caRNAs of the indicated 6-day-old seedlings. Expression levels are shown relative to those in the WT. *ACTIN2* is used as the internal control gene. The data are shown as mean ± s.e.m. (n = 4 independent experiments). The P values are from two-tailed Student's t-tests.

m^{6}A has less effect on the stability of retrotransposon RNAs

The increased abundance of m^{6}A retrotransposon RNAs may result from m^{6}A-meditated transcriptional and/or post-transcriptional regulation. Given its major effect on the lifetime of chromatin-associated regulatory RNA in mammals[15,19], we sought to determine whether m^{6}A could destabilize retrotransposon RNAs. We performed nuclear RNA decay assays using six-day-old WT, *vir* and *cpsf30-l* seedlings to sequence retrotransposon RNA levels after transcription inhibition

https://doi.org/10.1038/s41477-025-02137-z

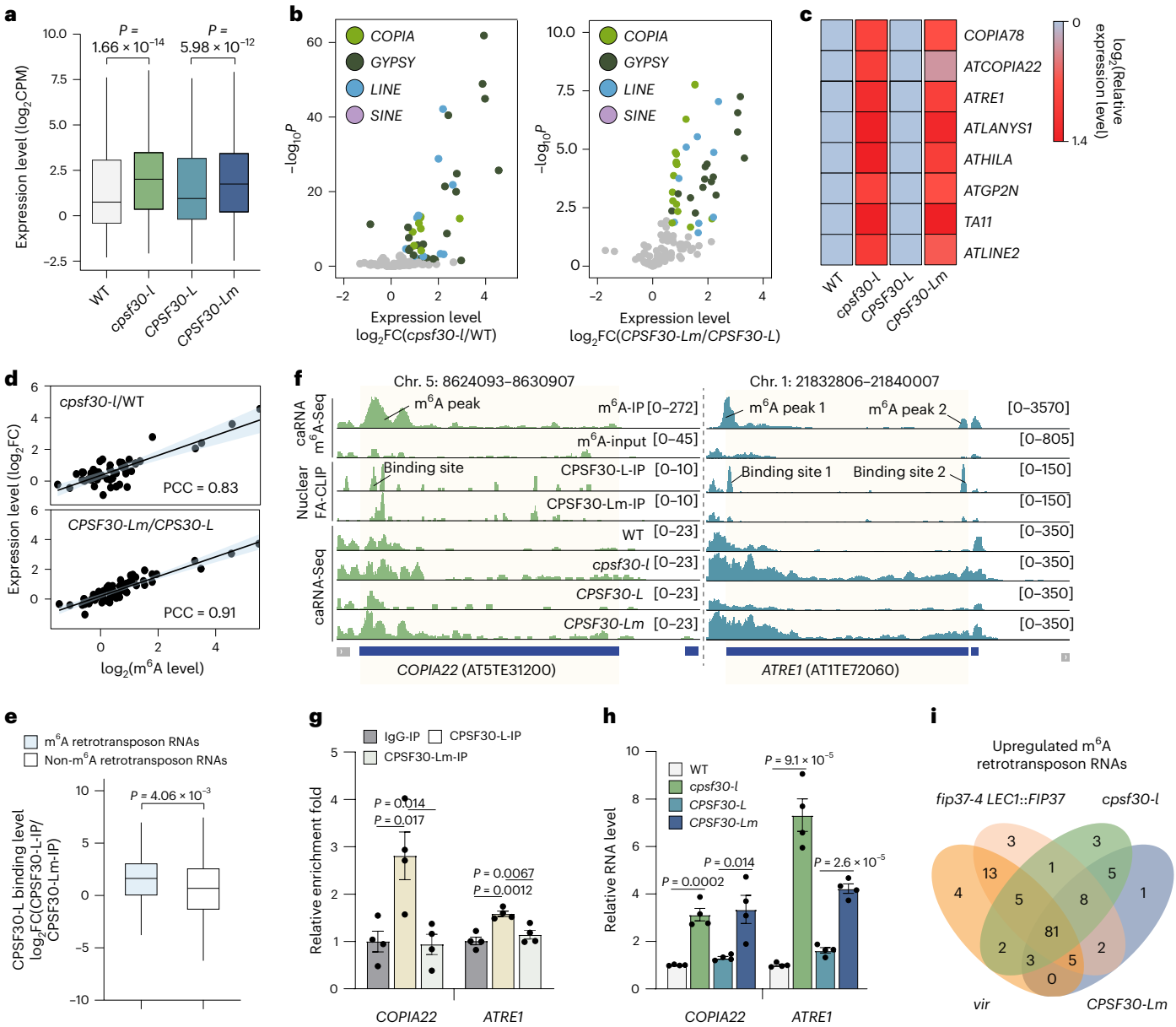

Fig. 3 | CPSF30-L binds and suppresses the expression of m^{6}A retrotransposon RNAs. a, Box plot showing the expression level of m^{6}A retrotransposon RNAs in WT, *cpsf30-l*, *CPSF30-L* and *CPSF30-Lm* seedlings. The medians (horizontal lines), interquartile ranges (boxes), and ±1.5× the interquartile range (whiskers) of the data are shown (n = 139 m^{6}A retrotransposon RNAs). P values were determined using paired two-sided Wilcoxon tests. **b**, Volcano plots illustrating the expression level changes of m^{6}A-marked retrotransposon RNAs in the paired comparisons of *cpsf30-l*/WT and *CPSF30-Lm*/*CPSF30-L*. Light green, dark green, blue and purple denote significantly dysregulated m^{6}A retrotransposon RNAs belonging to *COPIA*, *GYPSY*, *LINE* and *SINE*, respectively. Grey denotes non-differentially expressed m^{6}A retrotransposon RNAs. P values were calculated using a two-sided negative binomial generalized linear model from the count data. The threshold is $\log_2$FC > 0.58 with P < 0.05. **c**, Heat map showing changes of relative expression levels of the indicated m^{6}A retrotransposon subfamilies in WT, *cpsf30-l*, *CPSF30-L* and *CPSF30-Lm* seedlings. **d**, Scatter plots showing the positive correlation between m^{6}A level and expression change of m^{6}A retrotransposon RNAs in the paired comparisons of *cpsf30-l*/WT and *CPSF30-Lm*/*CPSF30-L*. The light-blue region indicates the 95% confidence interval. **e**, Box plot showing the CPSF30-L binding levels of m^{6}A and non-m^{6}A retrotransposon RNAs. The medians (horizontal lines), interquartile ranges (boxes), and ±1.5× the interquartile range (whiskers) of the data are shown (n = 57 detected m^{6}A retrotransposon RNAs and 373 detected non-m^{6}A retrotransposon RNAs). The P value was determined using a two-sided Wilcoxon test. **f**, Genomic visualization showing the normalized read densities of m^{6}A modifications, CPSF30-L binding levels and caRNA-Seq from the WT, *cpsf30-l*, *CPSF30-L* and *CPSF30-Lm* on the representative loci *COPIA22* and *ATRE1*. **g**, FA-RIP-qPCR showing the binding affinity of CPSF30-L to the *COPIA22* and *ATRE1* loci in 6-day-old *CPSF30-L* and *CPSF30-Lm* seedlings. AT2G07689 was used as the internal control gene. The data are shown as mean ± s.e.m. (n = 4 independent experiments). The P values are from two-tailed Student's t-tests. **h**, Relative expression levels of the *COPIA22* and *ATRE1* loci in the caRNAs of the indicated 6-day-old seedlings. Expression levels are shown relative to those in the WT. *ACTIN2* was used as the internal control gene. The data are shown as mean ± s.e.m. (n = 4 independent experiments). The P values are from two-tailed Student's t-tests. **i**, Venn diagram of upregulated m^{6}A retrotransposon RNAs after loss of function of CPSF30-L or depletion of m^{6}A writers.

https://doi.org/10.1038/s41477-025-02137-z

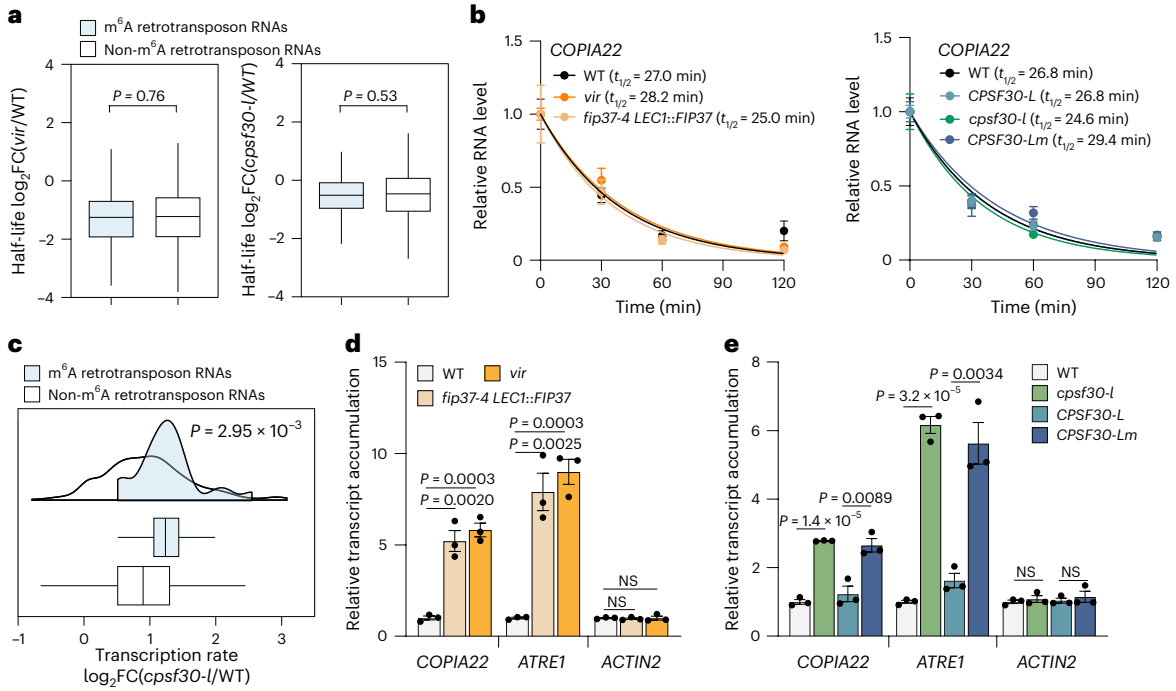

Fig. 4 | m^{6}A functions in transcriptional repression, but not stability, of retrotransposon RNAs. a, Box plots showing the half-life ratio (*vir*/WT and *cpsf30-l*/WT) of m^{6}A and non-m^{6}A retrotransposon RNAs. The medians (horizontal lines), interquartile ranges (boxes), and ±1.5× the interquartile range (whiskers) of the data are shown (n = 81 detected m^{6}A retrotransposon RNAs and 189 detected non-m^{6}A retrotransposon RNAs for *vir*/WT; n = 109 detected m^{6}A retrotransposon RNAs and 194 detected non-m^{6}A retrotransposon RNAs for *cpsf30-l*/WT). P values were determined using two-sided Wilcoxon tests. **b**, RT-qPCR showing the lifetime of *COPIA22* in the indicated seedlings treated with cordycepin at different time points. Relative RNA levels (normalized to spike-ins) are normalized to t = 0. $t_{1/2}$, half-life. The data are shown as mean ± s.e.m. (n = 3 independent experiments). **c**, Density plot and box plot showing the transcription rate difference between *cpsf30-l* and WT of m^{6}A and non-m^{6}A retrotransposon RNAs. The medians (horizontal lines), interquartile ranges (boxes), and ±1.5× the interquartile range (whiskers) of the data are shown (n = 25 detected m^{6}A retrotransposon RNAs and 699 detected non-m^{6}A retrotransposon RNAs). The P value was determined using a two-sided Wilcoxon test. **d**,**e**, Nuclear run-on assay showing that the transcription of *COPIA22* and *ATRE1* increases under either the depletion of m^{6}A writers (**d**) or the loss of function of an m^{6}A reader (**e**). Transcript accumulation levels are shown relative to that in the WT. *ACTIN2* was used as a negative control. The data are shown as mean ± s.e.m. (n = 3 independent experiments). The P values are from two-tailed Student's t-tests.

with cordycepin, and then calculated the half-life (Supplementary Tables 9 and 10). The half-life of m^{6}A retrotransposon RNAs was comparable to that of non-m^{6}A retrotransposon RNAs in both *vir* and *cpsf30-l* (Fig. 4a and Supplementary Fig. 5a). We also conducted nuclear RNA decay assays and measured the half-life of *COPIA22* following transcriptional inhibition with either cordycepin or actinomycin D. The results showed that neither m^{6}A removal nor the loss of m^{6}A recognition affected the half-life of *COPIA22* (Fig. 4b and Supplementary Fig. 5b). Given that the mammalian m^{6}A reader YTHDC1 associates with components of the nuclear exosome targeting complex and is involved in retrotransposon RNA degradation[15], we performed yeast two-hybrid (Y2H) assays and found that CPSF30-L does not directly interact with the nuclear exosome targeting components ZCCHC8A, ZCCHC8B and RBM7 (Supplementary Fig. 5c). These results suggest that m^{6}A on retrotransposon RNAs barely affects their stability and probably functions at the chromatin level.

m^{6}A silences the transcription of retrotransposon RNAs

The m^{6}A modification has been shown to affect chromatin-based transcriptional regulation[15,16,18]. To explore this further, we performed time-course RNA sequencing of nascent transcripts in six-day-old WT and *cpsf30-l* seedlings (Supplementary Table 11). Global analysis revealed that the transcription rates of m^{6}A retrotransposon RNAs were significantly upregulated in the *cpsf30-l* mutant relative to non-m^{6}A retrotransposon RNAs (Fig. 4c). Additionally, nuclear run-on assays in six-day-old WT, *fip37-4 LEC1*::*FIP37* and *vir* seedlings showed that the loss of m^{6}A caused a significant upregulation in the transcription rate of retrotransposon RNAs, such as *COPIA22* and *ATRE1* (Fig. 4d). The increased transcription rates of *COPIA22* and *ATRE1* were consistently observed in the *cpsf30-l* mutant, which was restored upon expressing CPSF30-L but not CPSF30-Lm (Fig. 4e). Together, these findings suggest that m^{6}A recognized by CPSF30-L suppresses the transcriptional activity of m^{6}A-modified retrotransposon RNAs in *Arabidopsis*.

m^{6}A on retrotransposon RNAs maintains local closed heterochromatin by enhancing the histone repressive modifications H3 K9 dimethylation and H3 K27 monomethylation

Transcriptional regulation is a complex and dynamic process in which histone modifications are a key component[40]. We first investigated the association of m^{6}A retrotransposon RNAs with heterochromatin and euchromatin histone modifications[41,42]. The calculated overlapping ratios (Jaccard statistics) showed that most m^{6}A retrotransposon RNAs were associated with two repressive heterochromatin modifications: dimethylation at H3 K9 and monomethylation at H3 K27, with rare associations with other repressive marks or euchromatin modifications (Supplementary Fig. 6a). Moreover, both dimethylated H3 K9 (H3K9me2) and monomethylated H3 K27 (H3K27me1) were highly enriched at the m^{6}A position on m^{6}A-modified retrotransposons (Fig. 5a). The methylation levels of H3 K9 and H3 K27 are significantly higher at the loci of m^{6}A retrotransposon RNAs than at non-m^{6}A ones (Supplementary Fig. 6b). The average m^{6}A peak densities are positively correlated with H3K9me2 and H3K27me1 levels on m^{6}A retrotransposon RNAs (Fig. 5b). These observations suggest that m^{6}A may play a role in heterochromatin in *Arabidopsis*. Immunostaining H3K9me2 and H3K27me1 in isolated nuclei from six-day-old seedlings revealed

a slight but clear reduction in their levels in *fip37-4 LEC1*::*FIP37*, *vir* and *cpsf30-l* (Fig. 5c,d). The reduced H3K9me2 and H3K27me1 signals in *cpsf30-l* could be restored by expressing *CPSF30-L* but not the m^{6}A-binding-function-abolished *CPSF30-Lm* (Fig. 5c,d), indicating that the m^{6}A binding function of CPSF30-L regulates H3K9me2 and H3K27me1 levels.

In plants, constitutive heterochromatin forms over repetitive elements, including retrotransposons, which are heavily decorated by H3K9me2 and H3K27me1. These repressive histone modifications prominently maintain heterochromatin integrity and silence transposons in *Arabidopsis*[24]. To further investigate whether and how m^{6}A contributes to the specialized establishment of heterochromatin states, we conducted genome-wide H3K9me2 with two biological replicates and H3K27me1 ChIP–Seq in six-day-old WT, *vir* and *cpsf30-l* seedlings (Supplementary Fig. 6c and Supplementary Tables 12 and 13). Compared with the reduced levels of H3K9me2 and H3K27me1 in their respective writer mutants, the loss of m^{6}A writer subunit *VIR* or m^{6}A reader *CPSF30-L* partially decreased these two histone modification levels (Supplementary Fig. 6d,e), consistent with the immunostaining results (Fig. 5c,d). Notably, H3K9me2 and H3K27me1 levels were significantly reduced on m^{6}A-modified retrotransposons and their subfamilies (Fig. 5e and Supplementary Fig. 6f), whereas no significant differences were observed in non-m^{6}A retrotransposons between *vir* and WT or *cpsf30-l* and WT plants (Supplementary Fig. 6g). To confirm these findings, we also performed ChIP-qPCR assays to examine the H3K9me2 and H3K27me1 levels on *COPIA22* and *ATRE1* in the genotypic plants. The results demonstrated that m^{6}A removal in m^{6}A writer mutants or the loss of m^{6}A recognition in *cpsf30-l* decreases H3K9me2 and H3K27me1 levels on *COPIA22* and *ATRE1* (Fig. 5f and Supplementary Fig. 6h). These results thus suggest that m^{6}A modulates H3K9me2 and H3K27me1 deposition at specific m^{6}A-modified retrotransposon regions.

Given that both repressive histone modifications, H3K9me2 and H3K27me1, are concurrently present on transposons[43], we speculated that they might synergistically contribute to the transcriptional silencing of m^{6}A retrotransposon RNAs. To address this, we analysed ChIP–Seq data in the WT and observed substantial overlap between H3K9me2 and H3K27me1 peaks (Supplementary Fig. 6i). Over 60% of m^{6}A retrotransposon RNAs harboured both modifications (termed H3K9me2 & H3K27me1 & m^{6}A retrotransposon RNAs; Supplementary Fig. 6j). Strikingly, *vir* and *cpsf30-l* mutants exhibited pronounced reductions in H3K9me2 and H3K27me1 levels at H3K9me2 & H3K27me1 & m^{6}A retrotransposon RNAs (Supplementary Fig. 6k). Moreover, lacking functions of either m^{6}A methylation or m^{6}A recognition leads to a greater increase in the expression of m^{6}A retrotransposon RNAs carrying both histone modifications compared with those marked by individual histone modifications (Supplementary Fig. 6l,m).

Considering that the decrease in repressive histone modifications potentially opens the chromatin state and influences nearby gene expression[44], we categorized the distance of genes to the nearest m^{6}A retrotransposon RNAs, ranging from 0 to 1 Mb, to explore the effect of m^{6}A regulation on neighbouring gene expression. The results showed that the expression of genes adjacent to m^{6}A retrotransposon RNAs tends to get lower as the distance increases in both *vir* and *cpsf30-l* mutants (Supplementary Fig. 7a), accompanied by gradually increased H3K9me2 and H3K27me1 levels (Supplementary Fig. 7b,c). However, these trends remained largely unchanged for non-m^{6}A retrotransposon RNAs (Supplementary Fig. 7d–f). These results indicate that the loss of deposition and recognition of m^{6}A compromises local and adjacent heterochromatin integrity and transcription.

The m^{6}A reader protein CPSF30-L associates with SUVH4/5/6 and ATXR5/6 and is required for H3K9me2/H3K27me1 levels at m^{6}A retrotransposons

We next investigated the mechanism underlying histone modifications and heterochromatin repression mediated by m^{6}A. Since H3K9me2 is methylated by SUVH4 (also known as KYP), SUVH5 and SUVH6 methyltransferases[45–48], and H3K27me1 is methylated by ATXR5 and ATXR6 (ref. 49), we analysed publicly available ChIP–Seq data for H3K9me2 and H3K27me1 in *suvh4 suvh5 suvh6* and *atxr5 atxr6* mutants[50,51]. Our analysis revealed a substantial reduction in H3K9me2 and H3K27me1 levels at the regions of m^{6}A-modified retrotransposons in *suvh4 suvh5 suvh6* and *atxr5 atxr6* (Supplementary Fig. 8a,b), confirming the roles of these methyltransferases in depositing H3K9me2 and H3K27me1 at the local regions of m^{6}A retrotransposon RNAs. Accordingly, we classified H3K9me2 peaks into two categories: SUVH4/5/6-dependent (decreased in *suvh4 suvh5 suvh6* mutants) and SUVH4/5/6-independent (unaltered in *suvh4 suvh5 suvh6* mutants). Similarly, H3K27me1 peaks were classified into ATXR5/6-dependent (decreased in *atxr5 atxr6* mutants) and ATXR5/6-independent (unaltered in *atxr5 atxr6* mutants). The depletion of *VIR* or *CPSF30-L* partially decreases SUVH4/5/6-dependent H3K9me2 and ATXR5/6-dependent H3K27me1 levels but has little effect on SUVH4/5/6-independent or ATXR5/6-independent peaks (Fig. 5g and Supplementary Fig. 8c), indicating that m^{6}A partially modulates H3K9me2 and H3K27me1 deposition via their respective methyltransferases.

As the deposition of H3K9me2 and H3K27me1 on retrotransposons requires heterochromatin targeting, we proceeded to investigate how m^{6}A spatially associates with heterochromatin to facilitate specialized methylation. Although no obvious differences in the expression levels of SUVH4/5/6 and ATXR5/6 were observed across WT, *fip37-4 LEC1*::*FIP37*, *vir* and *cpsf30-l* seedlings (Supplementary Fig. 8d), we observed that the expression levels of CPSF30-L were positively correlated with those of SUVH4/5 and ATXR5/6 (Supplementary Fig. 8e). Given that the depletion of m^{6}A writers and the m^{6}A reader CPSF30-L

Fig. 5 | m^{6}A affects heterochromatin state through CPSF30-L-mediated SUVH4/5/6-dependent H3K9me2 and ATXR5/6-dependent H3K27me1 deposition. a, Read-count tag density pile-ups of m^{6}A levels, H3K9me2 levels and H3K27me1 levels on m^{6}A retrotransposon RNAs. **b**, Scatter plots illustrating the positive correlation between m^{6}A levels and H3K9me2, as well as H3K27me1, levels in m^{6}A retrotransposon RNAs. The light-blue region indicates the 95% confidence interval. **c**, H3K9me2 and H3K27me1 immunostaining from 6-day-old WT, *fip37-4 LEC1*::*FIP37*, *vir*, *cpsf30-l*, *CPSF30-L* and *CPSF30-Lm* seedlings. Scale bars, 5 μm. The images are representative of three independent experiments. **d**, Quantification of H3K9me2 and H3K27me1 immunostaining in **c**; the intensity is normalized to the nuclear area. The data are shown as mean ± s.e.m. (n = 40, 40, 40, 40, 48 and 53 nuclei for H3K9me2 immunostaining and n = 43, 40, 40, 40, 40 and 40 nuclei for H3K27me1 immunostaining for each genotype from left to right). The P values are from two-tailed Student's t-tests. **e**, Read-count tag density pile-ups of H3K9me2 and H3K27me1 levels on m^{6}A retrotransposon RNAs in WT, *vir* and *cpsf30-l* seedlings. TSS, transcription start site; TES, transcription end site. **f**, ChIP-qPCR analysis of H3K9me2 and H3K27me1 levels at the *COPIA22* and *ATRE1* loci upon the loss of either m^{6}A writers or an m^{6}A reader. H3K9me2 and H3K27me1 levels are shown relative to that in the WT. The data are shown as mean ± s.e.m. (n = 3 independent experiments). The P values are from two-tailed Student's t-tests. **g**, Read-count tag density pile-ups of H3K9me2 levels on SUVH4/5/6-dependent peaks in WT, *suvh4 suvh5 suvh6*, *vir* and *cpsf30-l* seedlings, and H3K27me1 levels on ATXR5/6-dependent peaks in WT, *atxr5 atxr6*, *vir* and *cpsf30-l* seedlings. There were 3,897 SUVH4/5/6-dependent peaks and 8,961 ATXR5/6-dependent peaks. **h**, Y2H assay showing the interaction of CPSF30-L with SUVH4, SUVH5, SUVH6, ATXR5 and ATXR6 in yeast cells. The images are representative of two independent experiments. **i**, BiFC assay showing the physical interaction between CPSF30-L and SUVH4, SUVH5, SUVH6, ATXR5 and ATXR6 in *N. benthamiana* leaf cells. Scale bars, 5 μm. The images are representative of three independent experiments. **j**, Semi-in vivo pull-down assay showing the interaction of CPSF30-L with SUVH4, SUVH5, SUVH6, ATXR5 and ATXR6. The images are representative of two independent experiments.

https://doi.org/10.1038/s41477-025-02137-z

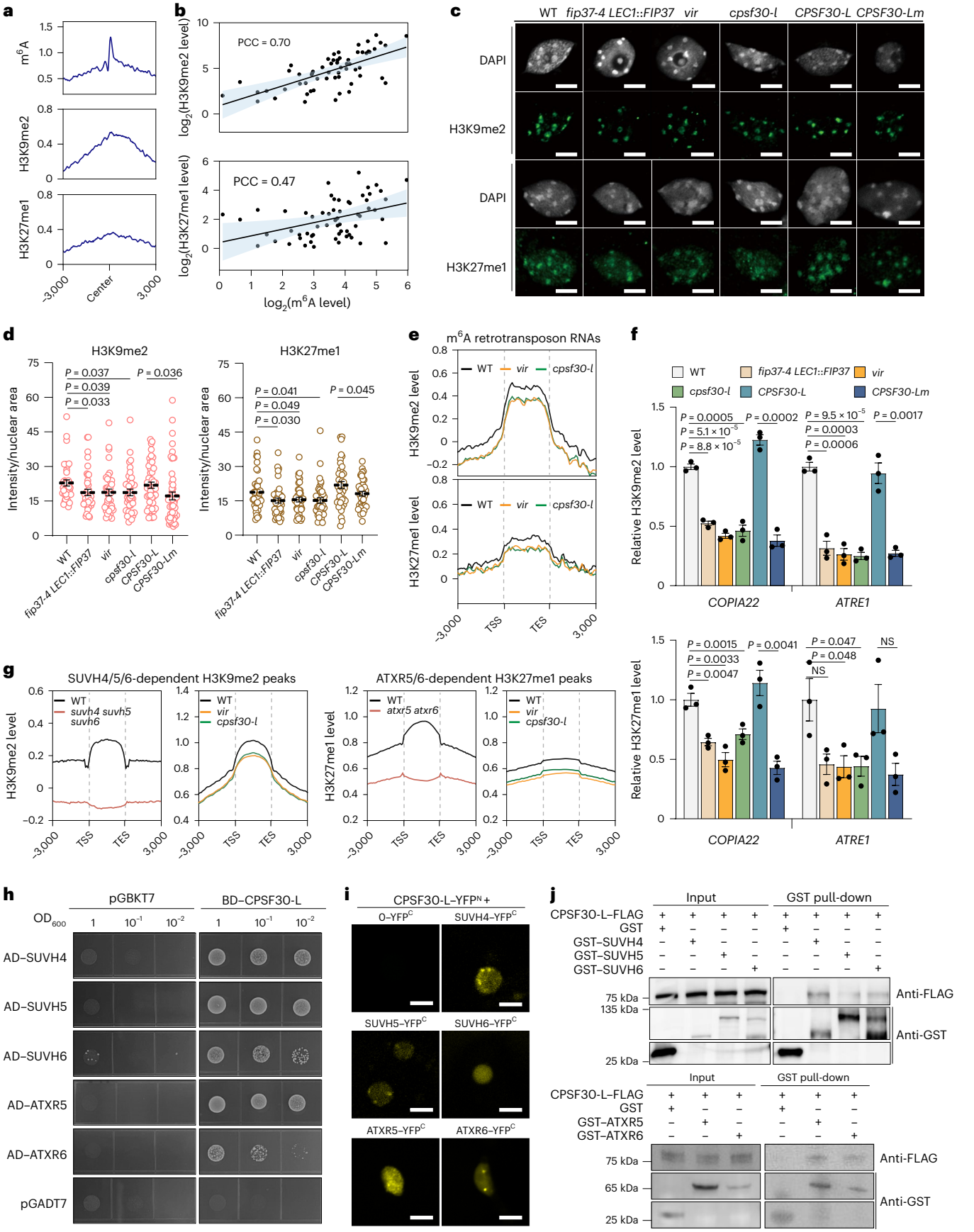

reduces H3K9me2 and H3K27me1 levels and enhances the transcription of m^{6}A-modified retrotransposons (Figs. 4c and 5e), we speculated that CPSF30-L, as an m^{6}A reader, might be responsible for m^{6}A-mediated transcriptional regulation through associating with SUVH4/5/6 and ATXR5/6 at specific loci for H3K9me2 and H3K27me1 deposition. To verify this hypothesis, we performed Y2H assays, revealing that CPSF30-L independently interacts with SUVH4/5/6 and ATXR5/6 (Fig. 5h). Bimolecular fluorescence complementation (BiFC) assays conducted in *Nicotiana benthamiana* leaves showed strong reconstituted YFP signal in the nucleus or nuclear foci among five protein pairs (Fig. 5i and Supplementary Fig. 8f). Moreover, semi-in vivo pull-down assays revealed that CPSF30-L–FLAG specifically binds glutathione S-transferase (GST)-targeted SUVH4/5/6 and ATXR5/6, but not GST alone (Fig. 5j). These interactions were not observed with m^{6}A writers (Supplementary Fig. 8g). Altogether, our findings provide evidence consistent with CPSF30-L acting as an intermediary linking m^{6}A to H3K9me2 and H3K27me1 deposition, thereby maintaining heterochromatin integrity in m^{6}A-modified retrotransposon RNA regions.

ECT12, as a nuclear m^{6}A reader, interacts with CPSF30-L and enhances the m^{6}A-binding function

Although disturbing either the deposition or recognition of m^{6}A impacts retrotransposon transcription, we noticed that partial m^{6}A hypomethylation on retrotransposons in *fip37-4 LEC1*::*FIP37* and *vir* mutants led to more pronounced expression increases in m^{6}A retrotransposon RNAs than in the *cpsf30-l* mutant (Supplementary Fig. 9a). These imbalanced effects caused by m^{6}A writers and an m^{6}A reader imply that other m^{6}A reader proteins may redundantly participate in this regulation. To identify the potential m^{6}A reader responsible for retrotransposon transcription in *Arabidopsis*, we conducted phylogenetic analysis comparing the identified metazoan YTHDC1 with its plant counterparts. This analysis revealed two putative homologues of YTHDC1 in *Arabidopsis*: CPSF30-L and ECT12 (AT4G11970; Supplementary Fig. 9b). Unlike other YTH-containing proteins, both CPSF30-L and ECT12 are exclusively localized in the nucleus (Supplementary Fig. 9c). Moreover, the mRNA expression level pattern of ECT12 strongly correlated with that of CPSF30-L (Supplementary Fig. 9d), indicating that they might have synergistic roles in biological and molecular process.

Given that ECT12 has been identified as a potential m^{6}A reader[52], we proceeded to elucidate its m^{6}A-binding function by performing an electrophoretic mobility shift assay with recombinant GST-tagged ECT12 (GST–ECT12) and a synthetic fluorescein-amidite-labelled RNA probe containing either m^{6}A or A. The electrophoretic mobility shift assay results revealed that ECT12 specifically binds m^{6}A-modified RNA but not unmethylated RNA (Supplementary Fig. 9e). Structural analysis of ECT12 identified conserved tryptophan residues at positions 94 and 144 as critical for m^{6}A recognition in the YTH domain. These residues form a hydrophobic aromatic cage, similar to those observed in other YTH domain proteins, such as YTHDC1 and CPSF30-L (Supplementary Fig. 9f). To verify that ECT12 depends on its YTH domain to recognize m^{6}A, we performed in vitro RIP followed by liquid chromatography–tandem mass spectrometry (LC–MS/MS) detection using the recombinant GST–ECT12, GST–ECT12/YTH and GST–ECT12/YTHm harbouring a putative non-m^{6}A binding alteration (W144A) with isolated *Arabidopsis* poly(A)$^+$ RNA. The LC–MS/MS results showed that m^{6}A was highly enriched in the immunoprecipitated fraction of GST–ECT12 and GST–ECT12/YTH, but not in the flow-through or the bound fraction of GST–ECT12/YTHm (Supplementary Fig. 9g), suggesting that the YTH domain is responsible for m^{6}A binding in ECT12. To further confirm that ECT12 indeed serves as an m^{6}A-binding protein in planta, we generated *ECT12*::*gECT12* and *ECT12*::*gECT12m* transgenic plants (Supplementary Fig. 9h), where ECT12m harbours the m^{6}A-binding-function-abolished alteration W144A, and then performed an in vivo RIP–LC–MS/MS assay. The results showed that ECT12 pulled down significantly more m^{6}A-modified RNAs than the control IgG-IP and ECT12m-IP (Fig. 6a). These results establish ECT12 as an m^{6}A reader protein in *Arabidopsis*. To investigate the potential spatial linkage between ECT12 and CPSF30-L, we examined transgenic *Arabidopsis* plants (*ECT12*::*gECT12-eGFP*) and found that ECT12 is localized in the nucleus (Supplementary Fig. 9h,i). We also performed Y2H and BiFC assays, confirming that ECT12 physically interacts with CPSF30-L, but not with m^{6}A writers (Fig. 6b,c and Supplementary Fig. 9j). Semi-in vivo pull-down assays also validated the interaction between CPSF30-L and ECT12 (Fig. 6d). To assess the regulatory role of the interaction between CPSF30-L and ECT12 in m^{6}A-modified RNAs, we conducted an in vitro RIP assay using purified recombinant CPSF30-L and ECT12 proteins along with poly(A)$^+$ RNAs. The results showed that CPSF30-L and ECT12 together bind significantly more m^{6}A-modified poly(A)$^+$ RNAs than the same amount of single CPSF30-L-IP and ECT12-IP (Fig. 6e). This indicates that the interaction between CPSF30-L and ECT12 enhances the m^{6}A-binding ability more effectively than the individual actions of CPSF30-L or ECT12 alone.

CPSF30-L and ECT12 redundantly mediate H3K9me2 and H3K27me1 formation and suppress the transcription of m^{6}A retrotransposon RNAs

Considering that CPSF30-L and ECT12 interact with each other as nuclear m^{6}A reader proteins, we proceeded to assess whether they redundantly regulate heterochromatic histone modifications and transcription of m^{6}A retrotransposon RNAs. To address this, we first characterized a homozygous transfer-DNA insertion mutant, *ect12-3* (SALK_071944), which almost completely disrupts the expression of full-length *ECT12* transcript (Supplementary Fig. 10a). We also generated *cpsf30-l ect12* double mutants using the CRISPR–Cas9 genome editing system, incorporating two guide RNAs targeting the second exonic region of *ECT12* in the *cpsf30-l* background (Supplementary Fig. 10a). We performed H3K9me2 and H3K27me1 immunostaining on these mutants to investigate whether ECT12 and CPSF30-L redundantly affect the methylation levels of these histone modifications. The results showed that the decrease in these two histone modification levels was less pronounced in *ect12-3* than in *cpsf30-l*, while the *cpsf30-l ect12* double mutants showed a more substantial reduction in these histone marks than either single mutant (Fig. 6f,g), consistent with genetic redundancy.

Consistent with these observations, ChIP–Seq analysis for H3K9me2 and H3K27me1 in six-day-old WT, *cpsf30-l*, *ect12-3* and *cpsf30-l ect12* seedlings also indicated redundant regulation of heterochromatic histone modifications (Supplementary Tables 12 and 13), particularly on m^{6}A retrotransposon RNAs, but not on non-m^{6}A retrotransposon RNAs (Fig. 6h and Supplementary Fig. 10b–f). These findings were corroborated by ChIP-qPCR targeting selected loci (Supplementary Fig. 10g). Consistently, the reduction in the levels of SUVH4/5/6-dependent H3K9me2 and ATXR5/6-dependent H3K27me1 in *cpsf30-l* was more pronounced in the *cpsf30-l ect12* double mutants (Fig. 6i and Supplementary Fig. 10h). Furthermore, no significant differences in the expression levels of SUVH4/5/6 and ATXR5/6 were detected across WT, *cpsf30-l*, *ect12-3* and *cpsf30-l ect12* seedlings, and no physical interaction was observed between ECT12 and SUVH4/5/6 or ATXR5/6 (Supplementary Fig. 10i,j). These results confirm that CPSF30-L and ECT12 form a complex to redundantly mediate H3K9me2 and H3K27me1 deposition.

To further elucidate how CPSF30-L and ECT12 redundantly regulate the expression of m^{6}A retrotransposon RNAs, we performed parallel caRNA-Seq on six-day-old WT, *cpsf30-l*, *ect12-3* and *cpsf30-l ect12* seedlings with two biological replicates (Supplementary Fig. 11a and Supplementary Table 14). Reflecting their shared involvement in regulating heterochromatic histone modifications, CPSF30-L and ECT12 collectively modulate the abundance of m^{6}A retrotransposon RNAs and

https://doi.org/10.1038/s41477-025-02137-z

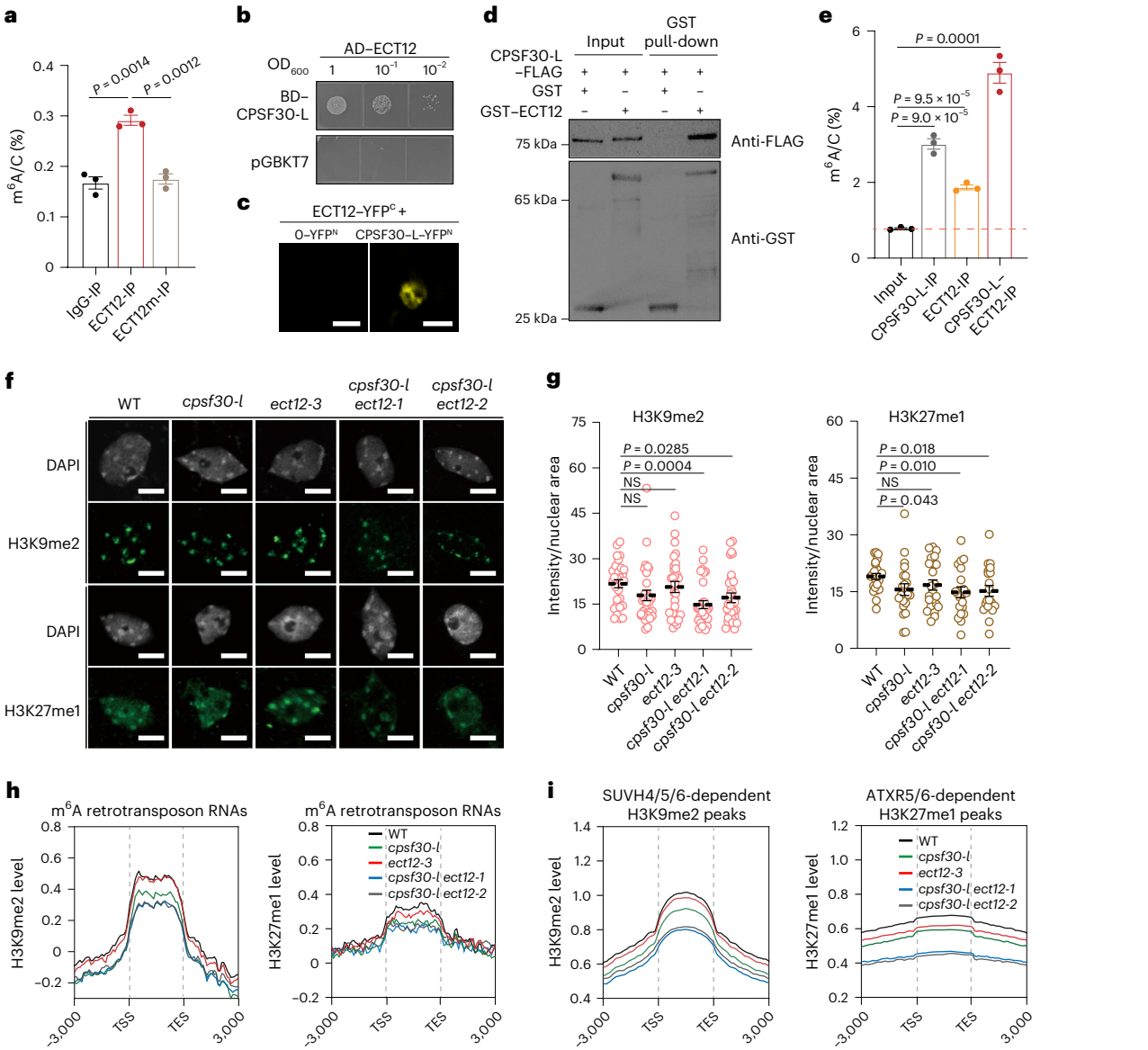

Fig. 6 | CPSF30-L and ECT12 redundantly mediate H3K9me2 and H3K27me1 deposition. a, In vivo nuclear FA-RIP–LC–MS/MS showing that m^{6}A is enriched in the ECT12-IP fraction compared with IgG-IP and the ECT12m-IP portion. The data are shown as mean ± s.e.m. (n = 3 independent experiments). The P values are from two-tailed Student's t-tests. **b**, Y2H assay showing the interaction of CPSF30-L with ECT12 in yeast cells. The images are representative of two independent experiments. **c**, BiFC assay showing the physical interaction between CPSF30-L and ECT12 in *N. benthamiana* leaf cells. Scale bars, 5 µm. The images are representative of three independent experiments. **d**, Semi-in vivo pull-down assay showing the interaction of CPSF30-L with ECT12. The images are representative of two independent experiments. **e**, In vitro RIP–LC–MS/MS showing m^{6}A levels in the input, CPSF30-L-IP, ECT12-IP and CPSF30-L–ECT12-IP RNA portions. m^{6}A levels are shown relative to those in the input. The data are shown as mean ± s.e.m. (n = 3 independent experiments). The P values are from two-tailed Student's t-tests. **f**, H3K9me2 and H3K27me1 immunostaining from 6-day-old WT, *cpsf30-l*, *ect12-3* and *cpsf30-l ect12* seedlings. Scale bars, 5 µm. The images are representative of three independent experiments. **g**, Quantification of H3K9me2 immunostaining in **f**; the intensity is normalized to the nuclear area. The data are shown as mean ± s.e.m. (n = 30, 31, 29, 31 and 31 nuclei for H3K9me2 immunostaining and n = 24, 21, 23, 20 and 20 nuclei for H3K27me1 immunostaining for each genotype from left to right). The P values are from two-tailed Student's t-tests. **h**, Read-count tag density pile-ups of H3K9me2 and H3K27me1 levels on m^{6}A retrotransposon RNAs in WT, *cpsf30-l*, *ect12-3* and *cpsf30-l ect12* seedlings. **i**, Read-count tag density pile-ups of H3K9me2 levels on SUVH4/5/6-dependent peaks and H3K27me1 levels on SUVH4/5/6-dependent peaks in WT, *cpsf30-l*, *ect12-3* and *cpsf30-l ect12* seedlings. There were 3,897 SUVH4/5/6-dependent peaks and 8,961 ATXR5/6-dependent peaks.

specific retrotransposon subfamilies, displaying genetic redundancy (Fig. 7a and Supplementary Fig. 11b,c). The *ect12-3* and *cpsf30-l* mutants exhibited significant increases in m^{6}A retrotransposon RNA expression, and *cpsf30-l ect12* double mutants showed more pronounced upregulation than either single mutant (Fig. 7a and Supplementary Fig. 11b,c). Overlapping the upregulated m^{6}A retrotransposon RNAs in *cpsf30-l*, *ect12-3* and *cpsf30-l ect12* demonstrated that virtually all of them were coordinately modulated by CPSF30-L and ECT12 (Fig. 7b). Further supporting this, we confirmed the significant elevation in the transcription and expression levels of *COPIA22* and *ATRE1* in *cpsf30-l ect12* mutants, with a twofold to tenfold increase compared with *cpsf30-l* or *ect12-3* mutants (Fig. 7c,d and Supplementary Fig. 11d). We also found that the changes in expression levels primarily followed a redundant trend, accompanied by a concurrent decrease in both H3K9me2 and H3K27me1 levels at H3K9me2 & H3K27me1 & m^{6}A retrotransposon RNA regions (Supplementary Fig. 11e,f). The disruption of m^{6}A nuclear

https://doi.org/10.1038/s41477-025-02137-z

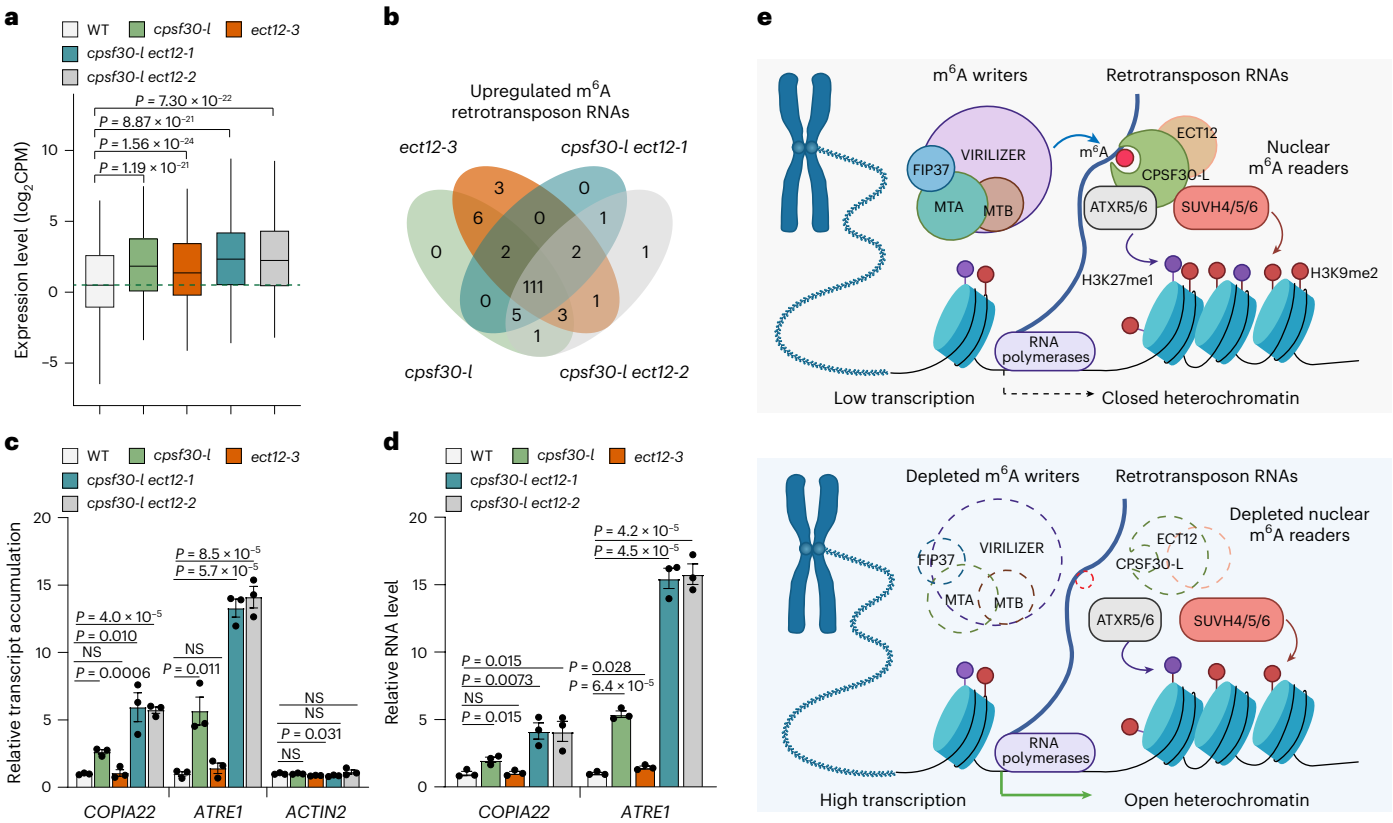

Fig. 7 | CPSF30-L and ECT12 cooperatively suppress the transcription and abundance of m^{6}A retrotransposon RNAs. a, Box plot showing the expression levels of m^{6}A retrotransposon RNAs in WT, *cpsf30-l*, *ect12-3* and *cpsf30-l ect12* seedlings. The medians (horizontal lines), interquartile ranges (boxes), and ±1.5× the interquartile range (whiskers) of the data are shown ($n = 139$ m^{6}A retrotransposon RNAs). *P* values were determined using paired two-sided Wilcoxon tests. **b**, Venn diagram of upregulated m^{6}A retrotransposon RNAs upon the depletion of individual m^{6}A readers and double m^{6}A readers. **c**,**d**, Relative transcriptional (**c**) and expression levels (**d**) of *COPIA22* and *ATRE1* in the indicated 6-day-old seedlings. *ACTIN2* is used as a negative and internal control. The data are shown relative to that in the WT. The data are shown as mean ± s.e.m. ($n = 3$ biological replicates). The *P* values are from two-tailed Student's *t*-tests. **e**, Hypothetical model depicting the mechanism of m^{6}A-mediated heterochromatin silencing of retrotransposons in *Arabidopsis*. m^{6}A on retrotransposon RNAs, deposited by m^{6}A writers, is recognized by CPSF30-L/ECT12 reader proteins, of which CPSF30-L recruits SUVH4/5/6 and ATXR5/6 to achieve repressive H3 K9 dimethylation and H3 K27 monomethylation, leading to closed heterochromatin and reduced transcription. Panel **e** created with BioRender.com.

readers led to a greater increase in the expression of m^{6}A retrotransposon RNAs carrying both histone modifications compared with those marked by a single modification (Supplementary Fig. 11f). Altogether, these results emphasize that CPSF30-L and ECT12 redundantly regulate H3K9me2 and H3K27me1 deposition, thereby suppressing the transcription of m^{6}A-modified retrotransposon RNAs.

Discussion

Our study unveils a comprehensive landscape of the RNA modification m^{6}A on caRNAs, especially in retrotransposon transcripts in *Arabidopsis*, revealing their transcriptional regulation via m^{6}A deposition and recognition with m^{6}A writer and reader proteins. Specifically, CPSF30-L and ECT12 form a complex to enhance m^{6}A binding affinity. CPSF30-L interacts with SUVH4/5/6 and ATXR5/6, together with ECT12, to facilitate H3K9me2 and H3K27me1 deposition at designated retrotransposons, achieving largely closed chromatin and repressed retrotransposons (Fig. 7e). These results highlight a new layer of epitranscriptomic regulation that modulates retrotransposon RNA transcription and maintains heterochromatin integrity.

It has been shown that m^{6}A promotes the decay of a subset of chromatin-associated regulatory RNAs, such as LINE1 in the nucleus of mouse embryonic stem cells[15]. Unlike the regulatory mechanism in mammals, our data show that m^{6}A modifications do not affect the stability of retrotransposon RNAs (Fig. 4a,b). Additionally, the lack of interaction between nuclear m^{6}A readers and nuclear exosome targeting components suggests that the m^{6}A-mediated regulatory mechanism primarily operates at the transcriptional level in plants (Supplementary Fig. 5c). This was further supported by increased transcription rates of m^{6}A retrotransposon RNAs in m^{6}A writer and reader mutants (Fig. 4c–e), implicating both evolutionarily conserved and divergent mechanisms of m^{6}A in transcriptional regulation.

We discovered that m^{6}A modifications are prevalent across various retrotransposon families and are particularly enriched at the 5′ and 3′ ends of transcripts (Fig. 1f). Disruption of the m^{6}A writer subunit in *fip37-4 LEC1*::*FIP37* and *vir* mutants significantly reduced m^{6}A levels on retrotransposon RNAs, leading to their increased abundance (Fig. 2a,b). This inverse relationship between m^{6}A methylation and RNA levels suggests that m^{6}A modification is crucial for suppressing retrotransposon expression. The investigation into the m^{6}A reader CPSF30-L revealed its essential role in binding m^{6}A-marked retrotransposons and suppressing their expression through m^{6}A recognition (Fig. 3).

We noticed that partial m^{6}A hypomethylation on retrotransposons in *fip37-4 LEC1*::*FIP37* and *vir* mutants led to more pronounced expression increases in m^{6}A retrotransposon RNAs than in the *cpsf30-l* mutant (Supplementary Fig. 9a). This disparity in effects, attributed to the mechanisms of m^{6}A writer and reader molecules, hints at the participation of additional m^{6}A reader proteins in a redundant regulatory capacity. Through phylogenetic analysis and molecular assays, we identified ECT12 as a nuclear m^{6}A reader that interacts with CPSF30-L and enhances its m^{6}A-binding function (Fig. 6a–e). The synergistic

action between CPSF30-L and ECT12 underscores the evolutionary significance of m^{6}A-mediated regulation, where multiple m^{6}A readers ensure robust transcriptional repression of retrotransposons.

Heterochromatic histone marks differ between mammals and plants. Although m^{6}A has been reported to regulate H3K9me3 deposition and heterochromatin states in mouse embryonic stem cells[16,18,26], it is necessary to investigate whether and how m^{6}A regulates heterochromatin state in plants. We observed that m^{6}A-modified retrotransposons were associated with heterochromatic marks H3K9me2 and H3K27me1 (Fig. 5a). Immunostaining results showed that the reduced H3K9me2 and H3K27me1 signals in *cpsf30-l* can be restored by expressing *CPSF30-L* but not by the m^{6}A-binding-function-abolished *CPSF30-Lm* (Fig. 5c,d), indicating that the m^{6}A binding function of CPSF30-L regulates H3K9me2 and H3K27me1 levels. In m^{6}A writer and reader mutants, we noted a notable reduction in H3K9me2 and H3K27me1 levels at m^{6}A retrotransposon loci (Fig. 5e). Compared with the reduced levels of H3K9me2 and H3K27me1 in their respective writer mutants (*suvh4 suvh5 suvh6* and *atxr5 atxr6*), the loss of m^{6}A writer subunit *VIR* or m^{6}A reader *CPSF30-L* only partially decreased these histone modifications (Supplementary Fig. 6d,e). This suggests that m^{6}A acts as a regulatory layer in modulating H3K9me2 and H3K27me1 deposition, specifically at m^{6}A-modified retrotransposon RNA regions. Mechanistically, CPSF30-L interacts with SUVH4/5/6 and ATXR5/6, the enzymes responsible for H3K9me2 and H3K27me1 deposition (Fig. 5h–j). This interaction links m^{6}A methylation with histone modification, maintaining a closed chromatin state and transcriptional repression of m^{6}A retrotransposon RNAs.

Besides histone modification, DNA methylation serves as another gene-silencing epigenetic mark. Heterochromatic non-CG methylation and H3 K9 dimethylation are interconnected through a cyclic reinforcement loop between the writers of non-CG DNA methylation and H3 K9 dimethylation[53,54]. In addition, DNA methylation is guided by small RNAs that target specific genomic sequences in a process known as RNA-directed DNA methylation, where Pol IV is required for short interfering RNA (siRNA) biogenesis and Pol V provides scaffold RNAs that guide siRNA-directed DNA methylation[55]. ChIP–Seq and caRNA-Seq analyses reveal that retrotransposon transcription is tightly regulated by the occupancy of Pol II and Pol V (Supplementary Fig. 2), suggesting a potential role for siRNAs and the involvement of Pol IV and Pol V in retrotransposon regulation. Furthermore, recent mammalian studies found that the m^{6}A reader FXR1 recruits DNA 5mC dioxygenase TET1 for 5mC demethylation in nearby genomic loci in normal and cancer cells, and the m^{6}A writer METTL3–METTL14 recruits DNA methyltransferase DNMT1 to chromatin for gene-body methylation[56,57], suggesting that m^{6}A could directly regulate DNA 5mC deposition. We therefore hypothesize that m^{6}A modification may also influence DNA methylation directly and siRNA-directed DNA methylation at retrotransposons apart from the H3K9me2-mediated DNA methylation pathway.

Retrotransposons account for over 40% of the human and mouse genomes, and their transcriptional regulation is essential for mammalian zygotic genome activation, embryonic stem cell identity and embryonic development[16,18,58]. Similarly, retrotransposons comprise an even more significant portion of crop plant genomes and can be transcriptionally activated by environmental challenges, promoting genetic diversity and adaptive evolutionary changes[59,60]. Here we found that the RNA modification m^{6}A is installed on retrotransposon RNAs to suppress their transcription, thereby securing genome integrity. It is worth investigating whether environmental challenges affect the installation of RNA modifications on retrotransposon RNAs. Besides m^{6}A, it is also important to explore whether other RNA modifications regulate retrotransposon RNAs in plants. Recently, the expression of FTO in rice was shown to increase field yield and biomass, accompanied by m^{6}A demethylation on repeat RNAs, enhanced chromatin accessibility and transcriptional activation[27]. This suggests that epitranscriptomic regulation in transcription represents a promising new avenue for plant breeding. Understanding how endogenous m^{6}A in plants modulates retrotransposon transcription and heterochromatin states could provide valuable insights for future crop improvement strategies.

Overall, our work demonstrates that m^{6}A co-transcriptionally directs heterochromatic histone modifications through its reader complexes, enabling a direct flow of RNA modification information from RNA to chromatin to ensure silenced transcription and heterochromatin integrity at m^{6}A-modified retrotransposon RNA regions. This regulatory interplay between the epitranscriptome and the epigenome provides deeper insights into m^{6}A functions as well as the mechanisms of retrotransposon regulation and heterochromatin maintenance in plant evolution and adaptation.

Methods

Plant materials and growth conditions

The WT *Arabidopsis thaliana* plants used in this study were of the Col-0 ecotype. *nrpe1-11*, *nrpb2-3*, *fip37-4 LEC1*::*FIP37*, *vir*, *cpsf30-l*, *CPSF30*::*CPSF30-L cpsf30-l* (*CPSF30-L*) and *CPSF30*::*CPSF30-Lm cpsf30-l* (*CPSF30-Lm*) have been described previously[3,4,10,33,34]. The *ect12-3* (SALK_071944) mutant lines were obtained from the *Arabidopsis* Biological Resource Center. Loss-of-function mutants of *cpsf30-l ect12* were generated using the CRISPR–Cas9 system. Specifically, two single guide RNA sequences targeting the *ECT12* gene were amplified via PCR, using the pDT1T2 vector as a template. The resulting products were purified, digested with BsaI and then ligated into the binary vector pHEE401E. Subsequently, the constructed plasmid was introduced into the *cpsf30-l* background through GV3101-mediated floral dipping. Positive seedlings were selected from 1/2× Murashige and Skoog plates containing 50 mg l^{-1} hygromycin B and confirmed via direct Sanger sequencing. All seeds of the WT and mutants were sterilized in 75% ethanol for 10 min followed by immersion in 20% bleaching solution for an additional 10 min, and immediately rinsed at least four times with sterile water. The sterilized seeds were stratified at 4 °C in darkness for three days and grown on 1/2× Murashige and Skoog nutrient agar plates. All plant germination and growth were under long-day conditions (16 h light/8 h dark at 22 °C with a light intensity of 90 to 120 µmol m^{-2} s^{-1}).

RT-qPCR

Isolated total RNAs and caRNAs were reverse-transcribed into first-strand cDNA using SuperScript III (Thermo Fisher Scientific) with random primers. The transcribed cDNAs were then appropriately diluted and used as templates for PCR reactions, employing Hieff qPCR SYBR Green Master Mix (Low Rox) from Yeasen. These reaction systems were subsequently analysed on a ViiA 7 instrument (Applied Biosystems) following the provided instructions. To ensure the accuracy of the results, each independent sample comprised at least three biological replicates and two technical replicates. A complete list of the primers used is provided in Supplementary Table 15.

Extraction of caRNAs

caRNAs were extracted using a previously reported method[61]. Briefly, 2 g of six-day-old seedlings were ground into a fine powder using liquid nitrogen. The powdered material was transferred into a 50-ml tube containing 10 ml of ice-cold Honda buffer (0.44 M sucrose, 1.25% (w/v) Ficoll, 2.5% (w/v) dextran T40, 20 mM HEPES-KOH pH 7.4, 10 mM $MgCl_2$, 0.5% (w/v) Triton X-100, 1 mM dithiothreitol (DTT), 1× protease inhibitor (Roche), 0.4 U µl^{-1} Ribolock RNase inhibitor (Thermo Fisher Scientific) and 100 ng µl^{-1} yeast tRNA (Invitrogen)). After homogenization via rotation, the homogenate was filtered through two layers of Miracloth (Merck). After centrifugation at 4 °C and 2,000 *g* for 5 min, the pellet was resuspended and washed with 5 ml of Honda buffer three or four times until the pellet appeared white. The washed

pellet was resuspended in 1 ml of Honda buffer and centrifuged at 4 °C and 8,000 *g* for 1 min. After the supernatant was removed, the nucleus pellet was weighed. One volume of nucleus resuspension buffer (50% (v/v) glycerol, 0.5 mM EDTA, 1 mM DTT, 25 mM Tris-HCl pH 7.5, 100 mM NaCl and 0.4 U μl^{-1} Ribolock RNase inhibitor (Thermo Fisher Scientific)) was added, and the pellet was stirred to mix with a pipette tip. Two volumes of washing buffer (25 mM Tris-HCl pH 7.5, 300 mM NaCl, 1 M urea, 0.5 mM EDTA, 1 mM DTT, 1% (v/v) Tween-20 and 0.4 U μl^{-1} Ribolock RNase inhibitor (Thermo Fisher Scientific)) were then added, and the pellet was washed by pipetting up and down 30 times and centrifuged at 4 °C and 8,000 *g* for 1 min. This washing procedure was repeated three times, and the pellet was retained as the chromatin-associated fraction. For RNA extraction, the pellet was resuspended in 1 ml of TRIzol (Invitrogen), and the extraction procedures were performed using the Direct-zol RNA Miniprep Plus kit with DNase digestion (ZYMO).

caRNA m^{6}A-Seq and m^{6}A-Seq

The caRNAs were concentrated with a ZYMO RNA Clean & Concentrator-5 kit (ZYMO) and processed for rRNA depletion according to the manufacturer's instructions (RiboPOOL). Then, 1 µl of 1:1,000 diluted m^{6}A spike-in from an EpiMark *N*^{6}-Methyladenosine Enrichment Kit (NEB) and 1:100 diluted ERCC spike-ins (Ambion) were added to 1 µg of rRNA-depleted caRNA, followed by fragmentation into 100–150 nucleotides using the Magnesium RNA Fragmentation Module (NEB). m^{6}A-IP was performed following the manufacturer's protocols. Library preparation was performed using a NEBNext Ultra II Directional RNA Library Prep Kit (NEB) according to the manufacturer's protocols. Sequencing was performed on an Illumina Novaseq machine in paired-end mode with 150 bp per read (Genewiz).

Poly(A)$^+$ RNA from six-day-old WT seedlings was applied to profile the m^{6}A methylome. 1 µg of poly(A)$^+$ RNA was fragmented into 100–150 nucleotides using the Magnesium RNA Fragmentation Module (NEB). m^{6}A-IP and library preparation were performed using the EpiMark *N*^{6}-Methyladenosine Enrichment Kit (NEB). Input and RNA eluted from m^{6}A-IP were used to prepare libraries with a NEBNext Ultra II Directional RNA Library Prep Kit (NEB). Sequencing was performed on an Illumina Novaseq machine in paired-end mode with 150 bp per read (Genewiz).

m^{6}A-IP–qPCR

For each biological replicate, 20 µg of caRNAs extracted from six-day-old *Arabidopsis* seedlings were supplemented with 1 µl of 1:100 diluted m^{6}A and non-m^{6}A spike-ins from the EpiMark *N*^{6}-Methyladenosine Enrichment Kit (NEB). The RNA samples were then fragmented using the Magnesium RNA Fragmentation Module (NEB), and the resulting fragments were subjected to IP with m^{6}A-conjugated antibodies bound to Protein G Dynabeads (Thermo Fisher Scientific), following the manufacturer's instructions. RNA was extracted from both the IP and input samples and analysed via RT-qPCR. The spike-ins served as normalization controls for m^{6}A level quantification. The primers used for qPCR are listed in Supplementary Table 15.

Nuclear FA-CLIP

For each biological replicate, 2 g of six-day-old seedlings were harvested and crosslinked with 1% (v/v) formaldehyde under vacuum. The crosslinking reaction was stopped after 15 min by adding glycine to a final concentration of 0.125 M, followed by an additional 5 min under vacuum. Nuclei were isolated from frozen, ground plant tissue using ice-cold Honda buffer (0.44 M sucrose, 1.25% (w/v) Ficoll, 2.5% (w/v) dextran T40, 20 mM HEPES-KOH pH 7.4, 10 mM $MgCl_2$, 0.5% (w/v) Triton X-100, 1 mM DTT, 1× protease inhibitor (Roche) and 0.4 U μl^{-1} Ribolock RNase inhibitor (Thermo Fisher Scientific)) and collected via centrifugation at 2,000 *g* for 5 min at 4 °C. The nuclei were washed twice with Honda buffer and resuspended in 1 ml of nuclear lysis buffer (150 mM KCl, 50 mM HEPES, pH 7.5, 2 mM EDTA, 1% (v/v) NP-40, 0.5 mM DTT, 1× protease inhibitor (Roche) and 40 U ml^{-1} RNase inhibitor (Thermo Fisher Scientific)). Sonication was performed using a Bioruptor (Diagenode) for four cycles (low power, 30 s pulse-on, 60 s pulse-off). After centrifugation, the supernatant was treated with 1 U μl^{-1} RNase T1 (Thermo Fisher Scientific) at 22 °C for 10 min and incubated with Anti-Flag M2 Magnetic beads (Sigma) with rotation at 4 °C for 3 h. The beads were washed three times with low-salt washing buffer (150 mM KCl, 50 mM HEPES, pH 7.5, 0.05% (w/v) NP-40, 0.5 mM DTT and 1× protease inhibitor (Roche)), followed by RNase T1 treatment and a second incubation at 22 °C for 10 min. After three additional washes with high-salt washing buffer (500 mM KCl, 50 mM HEPES, pH 7.5, 0.05% (w/v) NP-40, 0.5 mM DTT and 1× protease inhibitor (Roche)), the RNA underwent end repair and proteinase K digestion on beads. RNA was then recovered using the RNA Clean & Concentrator-5 Kit (Zymo), and libraries were prepared using the NEBNext Small RNA Library Prep Set (NEB). Sequencing was performed on the MGISEQ-2000 platform using a paired-end model (PE100).

In vivo FA-RIP-qPCR

Six-day-old *CPSF30*::*CPSF30-L-Flag cpsf30-1* and *CPSF30*::*CPSF30-Lm-Flag cpsf30-1* seedlings were separately fixed with 1% (v/v) formaldehyde solution. The fixed plant materials were ground into powder and incubated with lysis buffer (150 mM KCl, 50 mM HEPES, pH 7.5, 2 mM EDTA, 1% (v/v) NP-40, 1× protease inhibitor (Roche) and 40 U ml^{-1} Ribolock RNase inhibitor (Thermo Fisher Scientific)) in a head-over-tail rotation for 30 min at 4 °C. After full lysis and centrifugation, the lysates were collected and then immunoprecipitated with Anti-Flag M2 beads (Sigma-Aldrich) or a control IgG (CST) conjugated with protein G Dynabeads (Thermo Fisher Scientific) on a rotating wheel for 2 h at 4 °C. After washing, proteinase K digestion (NEB) and ethanol precipitation, the recovered RNA fractions were reverse-transcribed into cDNA to calculate the relative enrichment fold via RT-qPCR. AT2G07689 was used as the internal control.

Nuclear RNA lifetime sequencing

Six-day-old WT and mutant seedlings were placed in 3 ml of incubation buffer (15 mM sucrose, 1 mM KCl, 1 mM PIPES, pH 6.25 and 1 mM sodium citrate) in six-well plates (Corning Costar) and rotated at 600 *g* for 15 min. The initial (T_0) samples were promptly frozen, while the remaining samples underwent transcriptional inhibition by adding 3 ml of fresh buffer with 1 mM cordycepin (Macklin). Subsequently, the samples were subjected to three additional rounds of 1-min vacuum infiltration with 1-min decompression intervals. Samples were collected at various time points (15, 30, 60 and 120 min) after the third vacuum infiltration and frozen in liquid nitrogen. Approximately 0.2 g of seedlings per sample at each time point was used. The nuclear fraction was isolated, and total RNA was purified using Trizol (Invitrogen). Prior to purifying non-ribosomal RNA with the rRNA Depletion Kit (RiboPOOL), an equal amount of ERCC RNA spike-in control (Ambion) was added to the total nuclear RNA samples as internal controls. Library preparation was carried out using the NEBNext Ultra II Directional RNA Library Prep Kit (NEB). Sequencing was conducted on an Illumina Novaseq machine in paired-end mode with 150 bp per read (Genewiz).

Nuclear RNA lifetime measurement via qPCR

Six-day-old WT and mutant seedlings were placed in six-well plates containing 1 mM cordycepin (Macklin) or 200 µM Actinomycin D (Selleck). After three rounds of 1-min vacuum infiltration, samples were collected at 15, 30, 60 and 120 min. The nuclear fraction was isolated, and total RNA was extracted using Trizol (Invitrogen). Before RNA quantification via RT-qPCR, 1 µl of 1:100 diluted m^{6}A and non-m^{6}A spike-in from the EpiMark *N*^{6}-Methyladenosine Enrichment Kit (NEB) was introduced. The RNA degradation rate (k) was determined by plotting N_t/N_0 against time and fitting the equation $N_t/N_0 = e^{-kt}$, where

t represents transcription inhibition time, and N_t and N_0 indicate RNA quantities at time t and time 0. The RNA lifetime ($t_{1/2}$) was calculated as $t_{1/2} = (\ln 2)/k$.

Time-course RNA sequencing for transcription rate measurement

Six-day-old WT and *cpsf30-l* seedlings were placed in six-well plates containing 0.5 mM 5-ethynyl uridine (Jena Bioscience) and were collected at 30 min, 60 min and 120 min. Total RNA was purified using Trizol followed by rRNA depletion; nascent rRNA-depleted RNA was captured using a Click-iT Nascent RNA Capture Kit (Invitrogen). Before constructing libraries with a NEBNext Ultra II Directional RNA Library Prep Kit (NEB), an equal amount of ERCC RNA spike-in control (Ambion) was added to each sample. Sequencing was conducted on an Illumina Novaseq machine in paired-end mode with 150 bp per read (Genewiz).

Nuclear run-on assay

Six-day-old WT and mutant seedlings were ground into a fine powder in liquid N_2 and resuspended in 5 ml of pre-cooled nuclease-free Honda buffer. After filtering through two layers of Miracloth and centrifuging at 2,000 *g* for 10 min at 4 °C, the nuclei were washed two or three times with Honda buffer and resuspended in 50 µl of nucleus storage buffer (50 mM Tris-HCl, pH 7.8, 1 mM DTT, 20% (v/v) glycerol, 5 mM $MgCl_2$ and 0.44 M sucrose). The run-on assay was performed in a reaction containing 10 µl of 10× transcription assay buffer (500 mM Tris-HCl, pH 7.5, 50 mM $MgCl_2$, 1.5 M KCl, 1% (v/v) sarkosyl, 20 U ml^{-1} Ribolock RNase inhibitor (Thermo Fisher Scientific) and 100 mM DTT), 50 µl of nuclei in storage buffer, 5 µl of NTP mixture with BrUTP (100 mM ATP, 100 mM CTP, 100 mM GTP and 100 mM BrUTP (Sigma)) and 35 µl of H_2O. The run-on reaction was performed at 30 °C for 30 min. The reaction was stopped by adding 900 µl of TRIzol reagent (Invitrogen), and RNA was extracted using the Direct-zol RNA Miniprep Plus kit (ZYMO). The purified RNA was diluted in 500 µl of incubation buffer (20 mM Tris-HCl pH 7.5, 4 mM $MgCl_2$ and 0.2% (v/v) NP-40) and incubated with 60 µl of anti-BrdU beads (Santa Cruz) at 4 °C for 2 h. The precipitated RNA was extracted with TRIzol reagent (Invitrogen) and used for RT-qPCR analysis.

ChIP–Seq and ChIP-qPCR

The protocol for ChIP–Seq was adapted from a previously published method[62]. Briefly, 2 g of six-day-old WT, *cpsf30-l*, *ect12-3*, *cpsf30-l ect12-1*, *cpsf30-l ect12-2* and *vir* seedlings were ground with liquid nitrogen into fine powder and immediately fixed with 1% (v/v) formaldehyde. Nuclei were extracted and mononucleosomes were generated with micrococcal nuclease (MNase, NEB). Subsequently, MNase digestion was carried out and stopped with the addition of EDTA and EGTA to a final concentration of 10 mM. After centrifugation, the supernatant was diluted for IP. IP was conducted with anti-H3K9me2 (Abcam) and anti-H3K27me1 (Millipore) antibodies. After incubation overnight, Protein G Dynabeads (Thermo Fisher Scientific) were added to collect the immunocomplexes. After washing, elution, reverse crosslinking and DNA purification, recovered DNA and input were subjected to qPCR and library preparation with the NEXTflex Rapid DNA-Seq Kit for Illumina (PerkinElmer) according to the manufacturer's instructions and sequenced with the MGISEQ-2000 platform using a paired-end model (PE150).

Immunostaining

For immunostaining, 0.5 g of six-day-old seedlings were fixed with 4% paraformaldehyde for 20 min under vacuum. The fixed seedlings were then chopped in a petri dish containing 3 ml of ice-cold NEB1 buffer (10 mM Tris-HCl pH 9.5, 10 mM KCl, 500 mM sucrose and 0.1% Triton-X 100) to obtain a homogenate. The homogenate was filtered with a 40-µm cell strainer and centrifuged at 600 *g* for 3 min at 4 °C. The pellet was gently resuspended in 300 µl of NEB2 buffer (10 mM Tris-HCl, pH 9.5, 10 mM KCl, 125 mM sucrose and 0.1% Triton-X 100) and layered onto 600 µl of NEB3 buffer (10 mM Tris-HCl, pH 9.5, 10 mM KCl, 850 mM sucrose and 0.1% Triton-X 100). Nuclei were pelleted via centrifugation at maximum speed for 30 min at 4 °C, resuspended in 40 µl of NEB1 buffer and spread onto slides. The slides were air-dried, fixed with 4% paraformaldehyde for 30 min at room temperature and washed with PBST. Blocking was performed with 5% BSA for 1 h at 37 °C, followed by overnight incubation at room temperature with primary antibodies (1:100 anti-H3K27me1 (Abcam) and anti-H3K9me2 (Abcam)). After the PBST washes, the slides were incubated with secondary antibodies (1:100 Goat Anti-Mouse IgG H&L (Alexa Fluor 488, Abcam) and 1:100 Goat Anti-Rabbit IgG H&L (Alexa Fluor 555, Abcam)) for 1 h at 37 °C. Finally, the slides were washed with PBST, mounted with DAPI Fluoromount-G and imaged using a Zeiss LSM900 confocal microscope.

Y2H assay

The full-length coding sequences of *ZCCHC8A*, *ZCCHC8B*, *RBM7*, *SUVH4*, *SUVH5*, *SUVH6*, *ATXR5*, *ATXR6*, *CPSF30-L* and *ECT12* were fused in frame with the GAL4 activation domain in pGADT7 as prey. The full-length coding sequences of *CPSF30-L*, *ECT12*, *MTA*, *FIP37* and *VIR* with amino acid residues 1 to 1,470 (VIR^N) and 1,456 to 2,138 (VIR^C) were fused in frame with pGBKT7 as bait. Yeast strain Y2HGold cells were co-transformed with the bait and prey constructs. The empty vectors pGADT7 and pGBKT7 were co-transformed as the negative controls. Co-transformed yeast strain was spotted onto selective medium (minus His, Ade, Leu and Trp) and supplemented with the inhibitor of histidine synthesis 3-amino-1,2,4-triazole (Sigma). Images were taken after incubation for two to three days at 28 °C.

BiFC assay

The full-length coding sequences of *SUVH4*, *SUVH5*, *SUVH6*, *ATXR5*, *ATXR6*, *CPSF30-L* and *ECT12* were cloned into the binary pBI121–YFP^C or pBI121–YFP^N vector to generate SUVH4–YFP^C, SUVH5–YFP^C, SUVH6–YFP^C, ATXR5–YFP^C, ATXR6–YFP^C, ECT12–YFP^C and CPSF30-L–YFP^N constructs. The constructs with the indicated combinations were transiently co-expressed in *N. benthamiana* leaves via GV3101-mediated infiltration. The plants were grown in dark conditions for another two or three days, and the YFP fluorescence signal for each combination was detected using a confocal laser scanning microscope (ZESIS). Specifically, a 488-nm-wavelength laser was used to excite the YFP, with the emission signal collected from 500 to 550 nm.

Semi-in vivo pull-down assay

Total proteins were extracted from *Arabidopsis* seedlings expressing CPSF30-L–FLAG with IP buffer. 2 mg of total protein extracts were mixed with 20 µg of purified proteins infused with GST tag or GST alone. The mixture was incubated at 4 °C with gentle rotation for 2 h. After incubation, pre-washed Pierce Glutathione Magnetic Agarose Beads (Thermo Fisher Scientific) were added and incubated at 4 °C with gentle rotating for another 2 h. Proteins bound to the beads were eluted in elution buffer (125 mM Tris-HCl, pH 7.5, 150 mM NaCl, 1 mM EDTA, 1 mM DTT and 50 mM reduced glutathione) and were analysed via protein immunoblot with GST antibody (CST) and FLAG antibody (MCE).

Protein expression and purification

Plasmids containing GST–SUVH4, GST–SUVH5, GST–SUVH6, GST–ATXR5, GST–ATXR6, GST–ECT12, GST–ECT12/YTH, GST-ECT12/YTHm and MBP–CPSF30-L were transfected into *Escherichia coli* strain BL-21 Rosetta competent cells. Protein expression was induced at 18 °C with 1 mM isopropyl β-D-1-thiogalactopyranoside for 16 h. Cells were collected and resuspended in lysis buffer (10 mM Tris-HCl, pH 8.0, 500 mM NaCl, 1 mM PMSF, 3 mM DTT and 5% (v/v) glycerol), then lysed via sonication and centrifuged. The soluble proteins were first purified with either a GST-affinity column (GE Healthcare) or Amylose Resin

(NEB) and eluted using the corresponding elution buffer. The crude eluted fractions were further purified on a Superdex 75 exclusion column (GE Healthcare). The purified proteins were stored in storage buffer (10 mM Tris-HCl, pH 7.5, 200 mM NaCl, 3 mM DTT and 20% (v/v) glycerol) at −80 °C.

Electrophoretic mobility shift assay

The recombinant proteins GST–ECT12 were separately diluted to a series of concentrations ranging from 0 to 2 μM in binding buffer (10 mM HEPES-KOH, pH 8.0, 50 mM KCl, 1 mM EDTA, 0.05% (v/v) Triton X-100, 5% (v/v) glycerol, 10 μg ml^{-1} salmon DNA, 1 mM DTT and 40 U ml^{-1} Ribolock RNase inhibitor (Thermo Fisher Scientific)). Fluorescein-amidite-labelled RNA probe (4 nM final concentration) and 1 μl of protein were mixed in 10 μl of binding buffer and incubated on ice for 30 min. The entire RNA–protein mixture was loaded into a Novex 4–20% TBE gel (Thermo Fisher Scientific) for electrophoresis separation at 4 °C. The gel was visualized using ChemiDoc (Bio-Rad).

In vivo nuclear FA-RIP–LC–MS/MS

Nuclear RIP was conducted following a protocol similar to that for nuclear FA-CLIP, omitting the second RNase T1 digestion. Crosslinked six-day-old seedlings of *CPSF30*::*CPSF30-L cpsf30-l*, *CPSF30*::*CPSF30-Lm cpsf30-l*, *ECT12*::*gECT12 ect12-3* and *ECT12*::*gECT12m ect12-3* transgenic lines were subjected to IP using FLAG M2 Magnetic Beads (Sigma) or normal rabbit IgG (CST) bound to Protein G (Invitrogen). Crosslinked six-day-old WT seedlings were subjected to RIP using anti-Pol II antibody (Abcam) or IgG (CST) as a control. For GFP-tagged material, crosslinked *NRPE1*::*NRPE1-GFP/nrpe1* seedlings were immunoprecipitated using GFP-Trap Dynabeads (ChromoTek) or IgG (CST) as a control. After washing and RNA recovery, the m^6A levels in the RNA fractions were quantified via LC–MS/MS.

In vitro RIP–LC–MS/MS

For RIP–LC–MS/MS, 0.8 μg of poly(A)$^+$ RNA and the recombinant protein GST–ECT12 or MBP–CPSF30-L (final concentration 500 nM) were incubated in 200 μl of IPP buffer (150 mM NaCl, 0.1% (v/v) NP-40, 10 mM Tris-HCl, pH 7.5, 40 U ml^{-1} Ribolock RNase inhibitor (Thermo Fisher Scientific) and 0.5 mM DTT) with rotation at 4 °C for 2 h. Pre-equilibrated 10 μl of GST-affinity magnetic beads (Thermo Fisher Scientific) or amylose magnetic beads (NEB) with IPP buffer were added to each solution and incubated for an additional 2 h at 4 °C. The aqueous phase was harvested, recovered via ethanol precipitation and termed the flow-through. GST beads were washed four times with 200 μl of IPP buffer. The RNA on the beads was extracted with TRIzol reagent (Invitrogen) and saved as the recombinant protein-IP sample. LC–MS/MS was used to measure the ratio of m^6A/C in input, flow-through and recombinant protein-IP samples.

Quantification analysis via LC–MS/MS

LC–MS/MS analysis was performed as follows: RNA (around 100 to 200 ng) was digested with Nucleoside Digestion Mix (NEB) in 20 μl at 37 °C for 2 h. After centrifugation at maximum speed for 30 min, the aqueous phase containing nucleosides was separated using a LC pump (Shimadzu) equipped with a ZORBAX SB-Aq column (Agilent) and analysed via MS/MS on a Triple Quad 5500 mass spectrometer (AB SCIEX) in positive ion mode with multiple reaction monitoring. Nucleosides were quantified using the following mass transitions: 282.0 to 150.1 (m^6A), 244.0 to 112.0 (C). Quantification was based on a standard curve generated from pure nucleoside standards run alongside the samples. The ratios of m^6A/C were calculated using the calibrated concentrations.

Data analysis for caRNA-Seq and RNA-Seq

The sequencing data from the caRNA-Seq and RNA-Seq libraries were processed by trimming adapters with cutadapt (v.4.4)[63], followed by alignment to the TAIR10 reference genome via hisat2 (v.2.2.1)[64] with the following parameters: rna-strandness, FR; k, 10; pen-noncansplice, 1000000. We eliminated PCR duplicates using SAMtools in conjunction with Picard (v.21.0.1; https://broadinstitute.github.io/picard/)[65]. To enhance the authenticity and the repeatability of the results, we eliminated the transcript components of rRNA and tRNA, as well as those belonging to chloroplasts and mitochondria. Gene expression quantification was conducted using featureCounts (v.2.0.1)[66] and edgeR (v.3.36.0)[67] to compute counts, counts per million and differential gene expression. Therein, external ERCC spike-ins were also used to normalize the counts of each gene by using the R package RUVseq (v.1.28.0)[68]. The Pearson correlation was calculated using the R package cor (v.4.3.2)[69].

Data analysis for caRNA m^6A-Seq and m^6A-Seq

The analysis for the input group in caRNA m^6A-Seq or m^6A-Seq was conducted following the pipeline of RNA-Seq above. We employed cutadapt (v4.4)[63] for adapter trimming and size selection, retaining fragments that were 30 nucleotides or longer. These sequences were subsequently mapped to the TAIR10 reference genome using hisat2 (v.2.2.1)[64] with the default parameters. PCR duplicates were eliminated using SAMtools (v.1.13)[65] and Picard (v.21.0.1; https://broadinstitute.github.io/picard/). After obtaining the BAM files avoiding the reads classified to rRNA, tRNA, chloroplasts and mitochondria, we conducted a m^6A region enrichment analysis using MACS2 callpeak (v.2.2.7.1)[70] with the following settings: nomodel; shift, 25; extsize, 50; slocal, 200; llocal, 500; f, BAM; q, 0.05; g, 1.3e + 8. We considered regions exhibiting a false discovery rate below 0.05 for the analysis of m^6A peaks. Referring to the strategy and parameters used for m^6A peak calibration with IVT RNAs[71], we applied the same elimination rate criteria. If m^6A peaks appeared on retrotransposon RNAs in caRNA m^6A-Seq and did not overlap by more than 50% with those in m^6A-Seq, we considered these peaks as belonging to retrotransposon RNAs.

The m^6A level was calculated as previously described[16]. Specifically, to determine the m^6A level for each transcript in the WT, we first calculated the CPM using edgeR (v.3.36.0)[67]. The m^6A level was then derived using the formula (CPM_IP + 0.01)/(CPM_Input + 0.01). To account for differences in IP efficiency between WT and mutant samples, an equal amount of m^6A-modified spike-in RNA from the EpiMark N^6-Methyladenosine Enrichment Kit (NEB) was added to the rRNA-depleted caRNA samples of both the WT and mutants as an external control. For normalization across samples, the m^6A ratio of the spike-in (r_spike-in) was calculated as (CPM_IP-spike-in + 0.01)/(CPM_Input-spike-in + 0.01). The m^6A normalization factor (n.f.) for each mutant was defined as the ratio of r_spike-in in each mutant to the average r_spike-in across all WT samples. This factor corrects for differences in IP efficiency, and the final m^6A level for each mutant was determined using the formula (CPM_IP + 0.01)/(CPM_Input + 0.01)/n.f. The decrease in m^6A level was determined using the formula (m^6A level in WT − m^6A level in mutant)/(m^6A level in WT).

Data analysis for nuclear RNA stability assay

The data processing procedure to generate the BAM files mirrors the procedure we described above. Subsequent to this, gene expression quantification was performed using featureCounts (v.2.0.1)[66] and edgeR (v.3.36.0)[67] to compute counts normalized by ERCC and CPM at each time point. Setting the expression level at the initial time to 1, we fitted all degradation curves using the equation $y = \exp(-A \times x)$, where y is the relative expression level of a certain gene and x is the processing time. Subsequently, we eliminated genes with a value of A less than 0, derived from the fitting equation, from all sets of sequencing data. The half-lives of other genes were computed using the formula $t_{1/2} = (\ln 2)/A$.

Data analysis for time-course RNA sequencing

The procedure to generate the BAM files for each sample at different time points aligns with the pipeline we outlined above. Following this,

gene expression was finished using featureCounts (v.2.0.1)[66] and edgeR (v.3.36.0)[67] to calculate gene counts, normalized by ERCC and CPM at each respective time point. We fit all gene expression levels using a linear model represented as $y = A \times x + B$, where y signifies the expression level of a specific gene and x indicates the processing time. We then excluded genes with an A value less than 0, derived from the fitting equation, from all sequencing datasets. The transcription rate of a gene was represented by A.

Data analysis for ChIP–Seq

The alignment process was similar to that for other sequencing data including input groups and H3K9me2/H3K27me1 IP groups. H3K9me2/H3K27me1 peaks were identified using broad-peak mode in MACS2 (v.2.2.7.1)[70] with false discovery rate < 0.05. To assess the H3K9me2/H3K27me1 levels, heat maps and profile plots were generated using deepTools (v.3.5.1)[72]. The enrichment levels were normalized using reads per kilobase per million mapped reads to account for the differences between the IP and input datasets.

Statistics and reproducibility

The statistical tests performed on experimental data and the sample sizes are noted in the figure legends. All data points are derived from biological replicates.

Reporting summary

Further information on research design is available in the Nature Portfolio Reporting Summary linked to this article.

Data availability

The raw sequence data from caRNA m^{6}A-Seq, m^{6}A-Seq, caRNA-Seq, nuclear RNA lifetime sequencing, time-course RNA sequencing and ChIP–Seq reported in this paper have been deposited in the Genome Sequence Archive at the National Genomics Data Center, Beijing Institute of Genomics, Chinese Academy of Sciences, under accession number PRJCA037507; they are publicly accessible at https://bigd.big.ac.cn/gsa. All remaining data are provided in the main paper or the supplementary materials. Source data are provided with this paper.

References

1. Deng, X. et al. RNA N^6-methyladenosine modification in cancers: current status and perspectives. *Cell Res.* **28**, 507–517 (2018).
2. Zhong, S. et al. MTA is an *Arabidopsis* messenger RNA adenosine methylase and interacts with a homolog of a sex-specific splicing factor. *Plant Cell* **20**, 1278–1288 (2008).
3. Shen, L. et al. N^6-Methyladenosine RNA modification regulates shoot stem cell fate in *Arabidopsis*. *Dev. Cell* **38**, 186–200 (2016).
4. Růžička, K. et al. Identification of factors required for m^{6}A mRNA methylation in *Arabidopsis* reveals a role for the conserved E3 ubiquitin ligase HAKAI. *N. Phytol.* **215**, 157–172 (2017).
5. Martínez-Pérez, M. et al. *Arabidopsis* m^{6}A demethylase activity modulates viral infection of a plant virus and the m^{6}A abundance in its genomic RNAs. *Proc. Natl Acad. Sci. USA* **114**, 10755–10760 (2017).
6. Duan, H. C. et al. ALKBH10B is an RNA N^6-methyladenosine demethylase affecting *Arabidopsis* floral transition. *Plant Cell* **29**, 2995–3011 (2017).
7. Arribas-Hernández, L. et al. An m^{6}A–YTH module controls developmental timing and morphogenesis in *Arabidopsis*. *Plant Cell* **30**, 952–967 (2018).
8. Wei, L. H. et al. The m^{6}A reader ECT2 controls trichome morphology by affecting mRNA stability in *Arabidopsis*. *Plant Cell* **30**, 968–985 (2018).
9. Hou, Y. et al. CPSF30-L-mediated recognition of mRNA m^{6}A modification controls alternative polyadenylation of nitrate signaling-related gene transcripts in *Arabidopsis*. *Mol. Plant* **14**, 688–699 (2021).
10. Song, P. et al. *Arabidopsis* N^6-methyladenosine reader CPSF30-L recognizes FUE signals to control polyadenylation site choice in liquid-like nuclear bodies. *Mol. Plant* **14**, 571–587 (2021).
11. Wu, X. et al. N^6-Methyladenosine-mediated feedback regulation of abscisic acid perception via phase-separated ECT8 condensates in *Arabidopsis*. *Nat. Plants* **10**, 469–482 (2024).
12. Cai, Z. et al. The m^{6}A reader ECT8 is an abiotic stress sensor that accelerates mRNA decay in *Arabidopsis*. *Plant Cell* **36**, 2908–2926 (2024).
13. Song, P. et al. m^{6}A readers ECT2/ECT3/ECT4 enhance mRNA stability through direct recruitment of the poly(A) binding proteins in *Arabidopsis*. *Genome Biol.* **24**, 103 (2023).
14. Xu, C. et al. R-loop resolution promotes co-transcriptional chromatin silencing. *Nat. Commun.* **12**, 1790 (2021).
15. Liu, J. et al. N^6-Methyladenosine of chromosome-associated regulatory RNA regulates chromatin state and transcription. *Science* **367**, 580–586 (2020).
16. Wei, J. et al. FTO mediates LINE1 m^{6}A demethylation and chromatin regulation in mESCs and mouse development. *Science* **376**, 968–973 (2022).
17. Li, Y. et al. N^6-Methyladenosine co-transcriptionally directs the demethylation of histone H3K9me2. *Nat. Genet.* **52**, 870–877 (2020).
18. Liu, J. et al. The RNA m^{6}A reader YTHDC1 silences retrotransposons and guards ES cell identity. *Nature* **591**, 322–326 (2021).
19. Chelmicki, T. et al. m^{6}A RNA methylation regulates the fate of endogenous retroviruses. *Nature* **591**, 312–316 (2021).
20. Feschotte, C. Transposable elements and the evolution of regulatory networks. *Nat. Rev. Genet.* **9**, 397–405 (2008).
21. Lander, E. S. et al. Initial sequencing and analysis of the human genome. *Nature* **409**, 860–921 (2001).
22. Lanciano, S. & Cristofari, G. Measuring and interpreting transposable element expression. *Nat. Rev. Genet.* **21**, 721–736 (2020).
23. Jiao, Y. et al. Improved maize reference genome with single-molecule technologies. *Nature* **546**, 524–527 (2017).
24. Liu, C., Lu, F., Cui, X. & Cao, X. Histone methylation in higher plants. *Annu. Rev. Plant Biol.* **61**, 395–420 (2010).
25. Jambhekar, A., Dhall, A. & Shi, Y. Roles and regulation of histone methylation in animal development. *Nat. Rev. Mol. Cell Biol.* **20**, 625–641 (2019).
26. Xu, W. et al. METTL3 regulates heterochromatin in mouse embryonic stem cells. *Nature* **591**, 317–321 (2021).
27. Yu, Q. et al. RNA demethylation increases the yield and biomass of rice and potato plants in field trials. *Nat. Biotechnol.* **39**, 1581–1588 (2021).
28. Quesneville, H. Twenty years of transposable element analysis in the *Arabidopsis thaliana* genome. *Mob. DNA* **11**, 28 (2020).
29. Ream, T. S. et al. Subunit compositions of the RNA-silencing enzymes Pol IV and Pol V reveal their origins as specialized forms of RNA polymerase II. *Mol. Cell* **33**, 192–203 (2009).
30. Wierzbicki, A. T., Haag, J. R. & Pikaard, C. S. Noncoding transcription by RNA polymerase Pol IVb/Pol V mediates transcriptional silencing of overlapping and adjacent genes. *Cell* **135**, 635–648 (2008).
31. Böhmdorfer, G. et al. Long non-coding RNA produced by RNA polymerase V determines boundaries of heterochromatin. *eLife* **5**, e19092 (2016).
32. Zhai, J. et al. A one precursor one siRNA model for Pol IV-dependent siRNA biogenesis. *Cell* **163**, 445–455 (2015).

33. Zheng, B. et al. Intergenic transcription by RNA polymerase II coordinates Pol IV and Pol V in siRNA-directed transcriptional gene silencing in *Arabidopsis*. *Genes Dev.* **23**, 2850–2860 (2009).
34. Pontes, O. et al. The *Arabidopsis* chromatin-modifying nuclear siRNA pathway involves a nucleolar RNA processing center. *Cell* **126**, 79–92 (2006).
35. Liu, C. et al. *Arabidopsis* ARGONAUTE 1 binds chromatin to promote gene transcription in response to hormones and stresses. *Dev. Cell* **44**, 348–361.e347 (2018).
36. Liu, Y. et al. A conserved Pol II elongator SPT6L mediates Pol V transcription to regulate RNA-directed DNA methylation in *Arabidopsis*. *Nat. Commun.* **15**, 4460 (2024).
37. Shen, L. Functional interdependence of N^6-methyladenosine methyltransferase complex subunits in *Arabidopsis*. *Plant Cell* **35**, 1901–1916 (2023).
38. Wang, X. et al. N^6-Methyladenosine-dependent regulation of messenger RNA stability. *Nature* **505**, 117–120 (2014).
39. Wang, X. et al. N^6-Methyladenosine modulates messenger RNA translation efficiency. *Cell* **161**, 1388–1399 (2015).
40. Zaib, S., Rana, N. & Khan, I. Histone modifications and their role in epigenetics of cancer. *Curr. Med. Chem.* **29**, 2399–2411 (2022).
41. Luo, C., Durgin, B. G., Watanabe, N. & Lam, E. Defining the functional network of epigenetic regulators in *Arabidopsis thaliana*. *Mol. Plant* **2**, 661–674 (2009).
42. Antunez-Sanchez, J. et al. A new role for histone demethylases in the maintenance of plant genome integrity. *eLife* **9**, e58533 (2020).
43. Roudier, F. et al. Integrative epigenomic mapping defines four main chromatin states in *Arabidopsis*. *EMBO J.* **30**, 1928–1938 (2011).
44. Allshire, R. C. & Madhani, H. D. Ten principles of heterochromatin formation and function. *Nat. Rev. Mol. Cell Biol.* **19**, 229–244 (2018).
45. Du, J. et al. Mechanism of DNA methylation-directed histone methylation by KRYPTONITE. *Mol. Cell* **55**, 495–504 (2014).
46. Ebbs, M. L. & Bender, J. Locus-specific control of DNA methylation by the *Arabidopsis* SUVH5 histone methyltransferase. *Plant Cell* **18**, 1166–1176 (2006).
47. Ebbs, M. L., Bartee, L. & Bender, J. H3 lysine 9 methylation is maintained on a transcribed inverted repeat by combined action of SUVH6 and SUVH4 methyltransferases. *Mol. Cell. Biol.* **25**, 10507–10515 (2005).
48. Jackson, J. P., Lindroth, A. M., Cao, X. & Jacobsen, S. E. Control of CpNpG DNA methylation by the KRYPTONITE histone H3 methyltransferase. *Nature* **416**, 556–560 (2002).
49. Jacob, Y. et al. ATXR5 and ATXR6 are H3K27 monomethyltransferases required for chromatin structure and gene silencing. *Nat. Struct. Mol. Biol.* **16**, 763–768 (2009).
50. Li, X. et al. Mechanistic insights into plant SUVH family H3K9 methyltransferases and their binding to context-biased non-CG DNA methylation. *Proc. Natl Acad. Sci. USA* **115**, E8793–E8802 (2018).
51. Ma, Z. et al. *Arabidopsis* Serrate coordinates histone methyltransferases ATXR5/6 and RNA processing factor RDR6 to regulate transposon expression. *Dev. Cell* **45**, 769–784 (2018).
52. Amara, U., Hu, J., Park, S. J. & Kang, H. ECT12, an YTH-domain protein, is a potential mRNA m^6A reader that affects abiotic stress responses by modulating mRNA stability in *Arabidopsis*. *Plant Physiol. Biochem.* **206**, 108255 (2024).
53. Stroud, H. et al. Non-CG methylation patterns shape the epigenetic landscape in *Arabidopsis*. *Nat. Struct. Mol. Biol.* **21**, 64–72 (2014).
54. Law, J. A. & Jacobsen, S. E. Establishing, maintaining and modifying DNA methylation patterns in plants and animals. *Nat. Rev. Genet.* **11**, 204–220 (2010).
55. Matzke, M. A. & Mosher, R. A. RNA-directed DNA methylation: an epigenetic pathway of increasing complexity. *Nat. Rev. Genet.* **15**, 394–408 (2014).
56. Deng, S. et al. RNA m^6A regulates transcription via DNA demethylation and chromatin accessibility. *Nat. Genet.* **54**, 1427–1437 (2022).
57. Quarto, G. et al. Fine-tuning of gene expression through the Mettl3–Mettl14–Dnmt1 axis controls ESC differentiation. *Cell* **188**, 998–1018.e1026 (2025).
58. Li, X. et al. LINE-1 transcription activates long-range gene expression. *Nat. Genet.* **56**, 1494–1502 (2024).
59. Lisch, D. How important are transposons for plant evolution? *Nat. Rev. Genet.* **14**, 49–61 (2013).
60. Ito, H. et al. An siRNA pathway prevents transgenerational retrotransposition in plants subjected to stress. *Nature* **472**, 115–119 (2011).
61. Long, Y., Jia, J., Mo, W., Jin, X. & Zhai, J. FLEP-seq: simultaneous detection of RNA polymerase II position, splicing status, polyadenylation site and poly(A) tail length at genome-wide scale by single-molecule nascent RNA sequencing. *Nat. Protoc.* **16**, 4355–4381 (2021).
62. Xue, M. et al. The INO80 chromatin remodeling complex promotes thermomorphogenesis by connecting H2A.Z eviction and active transcription in *Arabidopsis*. *Mol. Plant* **14**, 1799–1813 (2021).
63. Martin, M. Cutadapt removes adapter sequences from high-throughput sequencing reads. *EMBnet.journal* **17**, 10–12 (2011).
64. Kim, D., Langmead, B. & Salzberg, S. L. HISAT: a fast spliced aligner with low memory requirements. *Nat. Methods* **12**, 357–360 (2015).
65. Li, H. et al. The Sequence Alignment/Map format and SAMtools. *Bioinformatics* **25**, 2078–2079 (2009).
66. Liao, Y., Smyth, G. K. & Shi, W. featureCounts: an efficient general purpose program for assigning sequence reads to genomic features. *Bioinformatics* **30**, 923–930 (2014).
67. Chen, Y., Lun, A. T. & Smyth, G. K. From reads to genes to pathways: differential expression analysis of RNA-Seq experiments using Rsubread and the edgeR quasi-likelihood pipeline. *F1000Res.* **5**, 1438 (2016).
68. Risso, D., Ngai, J., Speed, T. P. & Dudoit, S. Normalization of RNA-seq data using factor analysis of control genes or samples. *Nat. Biotechnol.* **32**, 896–902 (2014).
69. R Core Team. R: a language and environment for statistical computing. R package version 4.3.2. https://www.R-project.org/ (2025).
70. Zhang, Y. et al. Model-based analysis of ChIP-Seq (MACS). *Genome Biol.* **9**, R137 (2008).
71. Zhang, Z. et al. Systematic calibration of epitranscriptomic maps using a synthetic modification-free RNA library. *Nat. Methods* **18**, 1213–1222 (2021).
72. Ramírez, F., Dündar, F., Diehl, S., Grüning, B. A. & Manke, T. DeepTools: a flexible platform for exploring deep-sequencing data. *Nucleic Acids Res.* **42**, W187–W191 (2014).

Acknowledgements

We thank H. Yu (National University of Singapore), Y. Qi (Tsinghua University), B. Zheng (Fudan University) and C. Chen (Chinese Academy of Sciences) for providing the *fip37-4 LEC1*::*FIP37*, *nrpe1-11*, *nrpb2-3* and *NRPE1*::*NRPE1-GFP nrpe1* lines. We also thank the National Center for Protein Sciences at Peking University in Beijing, China, for assistance with sequencing, and G. Li for help with the MGI2000 experiment. This work was supported by the Biological Breeding-National Science and Technology Major Project of China (grant no. 2023ZD04073, G.J.), the National Key R&D Program of

China (grant no. 2024YFF1000302, G.J.) and the National Natural Science Foundation of China (grant nos. 22225704, 22477005 and 22321005, G.J.).

Author contributions

G.J. and P.S. conceived of the project. P.S. performed the experiments with the help of S.T., E.T., K.Y., L.L. and Z. Cai. Z. Cai, Z. Chen and P.S. analysed the sequencing data. G.J. and P.S. designed the experiments, interpreted the results and wrote the paper. All authors commented on the paper.

Competing interests

The authors declare no competing interests.

Additional information

Supplementary information The online version contains supplementary material available at https://doi.org/10.1038/s41477-025-02137-z.

Correspondence and requests for materials should be addressed to Guifang Jia.

Peer review information *Nature Plants* thanks Leandro Quadrana, Jixian Zhai and the other, anonymous, reviewer(s) for their contribution to the peer review of this work.

nature portfolio

Corresponding author(s): Guifang Jia

Last updated by author(s): Sep 10, 2025

Reporting Summary

Nature Portfolio wishes to improve the reproducibility of the work that we publish. This form provides structure for consistency and transparency in reporting. For further information on Nature Portfolio policies, see our Editorial Policies and the Editorial Policy Checklist.

Statistics

For all statistical analyses, confirm that the following items are present in the figure legend, table legend, main text, or Methods section.

n/a	Confirmed
☐	☒ The exact sample size (*n*) for each experimental group/condition, given as a discrete number and unit of measurement
☐	☒ A statement on whether measurements were taken from distinct samples or whether the same sample was measured repeatedly
☐	☒ The statistical test(s) used AND whether they are one- or two-sided *Only common tests should be described solely by name; describe more complex techniques in the Methods section.*
☒	☐ A description of all covariates tested
☒	☐ A description of any assumptions or corrections, such as tests of normality and adjustment for multiple comparisons
☐	☒ A full description of the statistical parameters including central tendency (e.g. means) or other basic estimates (e.g. regression coefficient) AND variation (e.g. standard deviation) or associated estimates of uncertainty (e.g. confidence intervals)
☐	☒ For null hypothesis testing, the test statistic (e.g. *F*, *t*, *r*) with confidence intervals, effect sizes, degrees of freedom and *P* value noted *Give P values as exact values whenever suitable.*
☒	☐ For Bayesian analysis, information on the choice of priors and Markov chain Monte Carlo settings
☒	☐ For hierarchical and complex designs, identification of the appropriate level for tests and full reporting of outcomes
☐	☒ Estimates of effect sizes (e.g. Cohen's *d*, Pearson's *r*), indicating how they were calculated

Our web collection on statistics for biologists contains articles on many of the points above.

Software and code

Policy information about availability of computer code

Data collection	QuantStudio TM 5 Real-Time System, 96-well (Applied Biosystem) was used for qPCR analysis. Images from immuno blotting were captured with a ChemDoc Imaging System (Bio-rad). The m6A content was measured using an Agilent 5500 Triple Quadrupole mass spectrometer (Agligent). The fluorescence signal was detected using LSM 900 confocal microscope (Zesis). The high-throughput sequencing was performed on the Illumina Novaseq 6000 and MGI2000 platform. Protein and DNA sequences of genes were downloaded from the Arabidopsis Information Resource (https:/www.arabidopsis.org).
Data analysis	Statistical analysis and plotting graph: GraphPad Prism (v9.0.0). Sequencing data mapping: hisat2 (v2.2.1) and Samtools (v1.13). RNA-Seq analysis: bedtools (v2.30.0); featureCounts (v2.0.1); R package edgeR (v3.36.0) and R package RUVseq (v1.28.0). m6A-Seq peak calling: macs2 callpeak (v2.2.7.1). ChIP-Seq analysis: deepTools (v3.5.1). Plots: R programming language (v4.3.2) with ggplot2 (v3.5.0), EnhancedVolcano (v1.20.0), ggvenn (v0.1.10) and pheatmap (v1.0.12).

For manuscripts utilizing custom algorithms or software that are central to the research but not yet described in published literature, software must be made available to editors and reviewers. We strongly encourage code deposition in a community repository (e.g. GitHub). See the Nature Portfolio guidelines for submitting code & software for further information.

Data

Policy information about availability of data

All manuscripts must include a data availability statement. This statement should provide the following information, where applicable:

- Accession codes, unique identifiers, or web links for publicly available datasets
- A description of any restrictions on data availability
- For clinical datasets or third party data, please ensure that the statement adheres to our policy

The raw sequence data of caRNA m6A-Seq, m6A-Seq, caRNA-Seq, nuclear RNA lifetime sequencing, time-course RNA sequencing, and ChIP-Seq reported in this paper have been deposited in the Genome Sequence Archive in National Genomics Data Center, Beijing Institute of Genomics (BIG), Chinese Academy of Sciences, under accession number PRJCA037507 that are publicly accessible at https://bigd.big.ac.cn/gsa. All remaining data are in the main paper or the supplementary materials. Source data are provided with this paper.

Research involving human participants, their data, or biological material

Policy information about studies with human participants or human data. See also policy information about sex, gender (identity/presentation), and sexual orientation and race, ethnicity and racism.

Reporting on sex and gender	Not applicable
Reporting on race, ethnicity, or other socially relevant groupings	Not applicable
Population characteristics	Not applicable
Recruitment	Not applicable
Ethics oversight	Not applicable

Note that full information on the approval of the study protocol must also be provided in the manuscript.

Field-specific reporting

Please select the one below that is the best fit for your research. If you are not sure, read the appropriate sections before making your selection.

☒ Life sciences ☐ Behavioural & social sciences ☐ Ecological, evolutionary & environmental sciences

For a reference copy of the document with all sections, see nature.com/documents/nr-reporting-summary-flat.pdf

Life sciences study design

All studies must disclose on these points even when the disclosure is negative.

Sample size	No statistical methods were used to predetermine sample sizes. The sample sizes for all experiments were estimated based on our prior experience with similar experiments and the appropriate sample sizes reported in relevant publications (Song et al., 2021, Molecular Plant, https://doi.org/10.1016/j.molp.2021.01.014; Cai et al., 2024, Plant Cell, https://doi.org/10.1093/plcell/koae149). The sample size for each experiment is fully described in the corresponding figure legends and/or Methods section. The chosen sample sizes were sufficient, and the experimental results were reproducible.
Data exclusions	No data were excluded.
Replication	All experiments were repeated at least 2-3 times with similar results, and the number of independent experiments or biological replicates is indicated in the figure legends and methods section.
Randomization	All samples were comparable based on genotypes, and collected randomly within same genotype for sequencing and other analyses. The growth conditions for plant materials are described in the method section.
Blinding	Blinding was not applicable in this study because the experimental subjects were plants, and the investigators were necessarily aware of the genotypes being handled. Moreover, to ensure data reliability, all experiments included appropriate positive and negative controls, and the consistency of results across multiple independent biological replicates further minimized potential experimental bias. Therefore, blinding was not relevant in this context.

Reporting for specific materials, systems and methods

We require information from authors about some types of materials, experimental systems and methods used in many studies. Here, indicate whether each material, system or method listed is relevant to your study. If you are not sure if a list item applies to your research, read the appropriate section before selecting a response.

Materials & experimental systems

n/a	Involved in the study
☐	☒ Antibodies
☒	☐ Eukaryotic cell lines
☒	☐ Palaeontology and archaeology
☒	☐ Animals and other organisms
☒	☐ Clinical data
☒	☐ Dual use research of concern
☐	☒ Plants

Methods

n/a	Involved in the study
☐	☒ ChIP-seq
☒	☐ Flow cytometry
☒	☐ MRI-based neuroimaging

Antibodies

Antibodies used

Anti-H3 (Abcam, Cat# ab1791, 1:2000 dilution)
Anti-UGPase (Agrisera, Cat# AS05 086, 1:2000 dilution)
Anti-H3K9me2 (Abcam, Cat# ab1220, 1:1000 dilution)
Anti-H3K27me1 (Milipore, Cat# 07-448, 1:1000 dilution)
Anti-Pol II (Abcam, Cat# ab26721, 1:1000 dilution)
Anti-FLAG (MedChemExpress, Cat# HY-P80111, 1:2000 dilution)
Goat Anti-Mouse IgG H&L (Alexa Fluor® 488, Abcam, Cat# ab150113, 1:100 dilution)
Goat Anti-Rabbit IgG H&L (Alexa Fluor® 555, Abcam, Cat# ab150078, 1:100 dilution)
Anti-GST (Cell Signaling Technology, Cat# 2622, 1:2000 dilution)

Validation

The validation statements for the species and application of all the commercial antibodies used in this study can be found in the manufacturers' websites as follows.
Anti-H3 (Abcam, ab1791): https://www.abcam.cn/products/primary-antibodies/histone-h3-antibody-nuclear-marker-and-chip-grade-ab1791.html
Anti-UGPase (Agrisera, AS05 086): https://www.agrisera.com/en/artiklar/ugpase-udp-glucose-pyrophosphorylase-marker-of-cytoplasm.html
Anti-H3K9me2 (Abcam, ab1220): https://www.abcam.cn/products/primary-antibodies/histone-h3-di-methyl-k9-antibody-mabcam-1220-chip-grade-ab1220.html
Anti-H3K27me1 (Milipore, 07-448): https://www.sigmaaldrich.cn/CN/zh/product/mm/07448
Anti-Pol II (Abcam, ab26721): https://www.abcam.cn/products/primary-antibodies/rna-polymerase-ii-ctd-repeat-ysptsps-antibody-chip-grade-ab26721.html
Anti-FLAG (MedChemExpress, HY-P80111): https://www.medchemexpress.cn/antibody/dykddddk-tag-flag-mouse-mab.html
Anti-GST (Cell Signaling Technology, 2622): https://www.cellsignal.cn/products/primary-antibodies/gst-tag-antibody/2622

Dual use research of concern

Policy information about dual use research of concern

Hazards

Could the accidental, deliberate or reckless misuse of agents or technologies generated in the work, or the application of information presented in the manuscript, pose a threat to:

No	Yes
☒	☐ Public health
☒	☐ National security
☒	☐ Crops and/or livestock
☒	☐ Ecosystems
☒	☐ Any other significant area

Experiments of concern

Does the work involve any of these experiments of concern:

No	Yes	
☒	☐	Demonstrate how to render a vaccine ineffective
☒	☐	Confer resistance to therapeutically useful antibiotics or antiviral agents
☒	☐	Enhance the virulence of a pathogen or render a nonpathogen virulent
☒	☐	Increase transmissibility of a pathogen
☒	☐	Alter the host range of a pathogen
☒	☐	Enable evasion of diagnostic/detection modalities
☒	☐	Enable the weaponization of a biological agent or toxin
☒	☐	Any other potentially harmful combination of experiments and agents

Plants

Seed stocks	Arabidopsis cpsf30-l and ect12-3 seeds were obtained from Arabidopsis Biological Resource Center with accession GK_477H04_019132 and SALK_071944, respectively. Arabidopsis nrpb2-3 seeds were obtained from published search group (https://genesdev.cshlp.org/content/23/24/2850). Arabidopsis nrpe1-11 seeds were obtained from published search group (https://www.sciencedirect.com/science/article/pii/S0092867406007537). Arabidopsis LEC1:FIP37/fip37-4 seeds were obtained from published search group (https://doi.org/10.1016/j.devcel.2016.06.008). Arabidopsis vir seeds were obtained from published search group (https://doi.org/10.1111/nph.14586). Arabidopsis NRPE1:NRPE1-GFP/nrpe1 seeds were obtained from published search group (https://www.nature.com/articles/s41467-024-48940-8).
Novel plant genotypes	Arabidopsis cpsf30-l/ect12 mutants were generated by CRISPR-CAS9
Authentication	The genotype of nrpb2-3, nrpe1-11, LEC1:FIP37/fip37-4, vir, cpsf30-l, ect12-3, cpsf30-l/ect12-1, cpsf30-l/ect12-2 were confirmed by genotyping or sanger sequencing.

ChIP-seq

Data deposition

☒ Confirm that both raw and final processed data have been deposited in a public database such as GEO.

☐ Confirm that you have deposited or provided access to graph files (e.g. BED files) for the called peaks.

Data access links *May remain private before publication.*	The raw sequence data of ChIP-Seq reported in this paper have been deposited in the Genome Sequence Archive in National Genomics Data Center, Beijing Institute of Genomics (BIG), Chinese Academy of Sciences, under accession number PRJCA037507 that are publicly accessible at https://bigd.big.ac.cn/gsa.
Files in database submission	6-d-old-H3K9me2-ChIP-WT-IP-1 6-d-old-H3K9me2-ChIP-WT-IP-2 6-d-old-H3K9me2-ChIP-cpsf30-l-IP-1 6-d-old-H3K9me2-ChIP-cpsf30-l-IP-2 6-d-old-H3K9me2-ChIP-ect12-3-IP-1 6-d-old-H3K9me2-ChIP-ect12-3-IP-2 6-d-old-H3K9me2-ChIP-cpsf30-ect12-2-IP-1 6-d-old-H3K9me2-ChIP-cpsf30-ect12-2-IP-2 6-d-old-H3K9me2-ChIP-cpsf30-ect12-1-IP-1 6-d-old-H3K9me2-ChIP-cpsf30-ect12-1-IP-2 6-d-old-H3K9me2-ChIP-vir-IP-1 6-d-old-H3K9me2-ChIP-vir-IP-2 6-d-old-H3K9me2-ChIP-WT-Input-1 6-d-old-H3K9me2-ChIP-WT-Input-2 6-d-old-H3K9me2-ChIP-cpsf30-l-Input-1 6-d-old-H3K9me2-ChIP-cpsf30-l-Input-2 6-d-old-H3K9me2-ChIP-ect12-3-Input-1 6-d-old-H3K9me2-ChIP-ect12-3-Input-2 6-d-old-H3K9me2-ChIP-cpsf30-l-ect12-1-Input-1 6-d-old-H3K9me2-ChIP-cpsf30-l-ect12-1-Input-2 6-d-old-H3K9me2-ChIP-cpsf30-l-ect12-2-Input-1 6-d-old-H3K9me2-ChIP-cpsf30-l-ect12-2-Input-2 6-d-old-H3K9me2-ChIP-vir-Input-1 6-d-old-H3K9me2-ChIP-vir-Input-2 6-d-old-H3K27me1-ChIP-WT-IP-1 6-d-old-H3K27me1-ChIP-WT-Input-1 6-d-old-H3K27me1-ChIP-vir-IP-1 6-d-old-H3K27me1-ChIP-vir-Input-1

6-d-old-H3K27me1-ChIP-ect12-3-IP-1
6-d-old-H3K27me1-ChIP-ect12-3-Input-1
6-d-old-H3K27me1-ChIP-cpsf30-l-IP-1
6-d-old-H3K27me1-ChIP-cpsf30-l-Input-1
6-d-old-H3K27me1-ChIP-cpsf30-l-ect12-2-IP-1
6-d-old-H3K27me1-ChIP-cpsf30-l-ect12-1-IP-1
6-d-old-H3K27me1-ChIP-cpsf30-ect12-2-Input-1
6-d-old-H3K27me1-ChIP-cpsf30-ect12-1-Input-1

Genome browser session
(e.g. UCSC)

No public available genome browser session.

Methodology

Replicates

Two biological replicates for H3K9me2 and one biological replicate for H3K27me1 ChIP-seq.

Sequencing depth

At least 36 million pair-end (2*150bp) raw reads on average for each experiment.

Antibodies

H3K9me2 monoclonal antibody (Abcam, ab1220)
H3K27me1 monoclonal antibody (Milipore, Cat# 07-448)

Peak calling parameters

macs2 callpeak -t <IP files> -c <Input files> --broad -f BAM -n <output peak file> -q 0.05 -g 1.3e+8 -m 5 100 --keep-dup all

Data quality

Thousands of confidential H3K9me2 and H3K27me1 peaks were obtained under the threshold of FDR < 0.05 and fold enrichment > 5 from each genotype.

Software

The sequencing data were first processed using cutadapt (v4.4) to trim adapters, followed by alignment to the TAIR10 reference genome (https://www.arabidopsis.org) via hisat2 (v2.2.1). We eliminated PCR duplicates using Samtools (v1.13) in conjunction with Picard. Fold-enrichment heatmaps and profiles of H3K9me2 and H3K27me1 were generated by deepTools software (v3.5.1).